Contents lists available at ScienceDirect

Applied Catalysis B: Environment and Energy

An all-in-one self-supporting Na-Bi$_2$WO$_6$ photocatalyst for portable air purifier: Laminar splitting boosts high efficacy in mineralizing toluene and disinfection

Mingxia Lu [a], Lixia Yang [a,*], Ziyi Wu [a], Qi Wang [b], Menglei Wang [a], Jiajian Xu [c], Shuqu Zhang [a], Renjie Song [a], Weili Dai [a], Jianping Zou [a], Shenglian Luo [a]

[a] *Key Laboratory of Jiangxi Province for Persistent Pollutants Control and Resources Recycle, Nanchang Hangkong University, Nanchang, Jiangxi Province 330063, China*
[b] *School of Measuring and Optical Engineering, Nanchang Hangkong University, Nanchang, Jiangxi Province 330063, China*
[c] *School of art and design, Nanchang Hangkong University, Nanchang, Jiangxi Province 330063, China*

ARTICLE INFO

ABSTRACT

An air purifier that provides clean air will be popular if it is portable and capable of removing volatile organic chemicals and reducing exposure to bacteria. Herein, ultra-thin and dense Bi$_2$WO$_6$ nanoflakes grown on W meshes specialize in offering abundant oxygen vacancies due to Na$^+$ driving laminar splitting. Under visible lights, the photogenerated carriers streaming along the ultrathin Bi$_2$WO$_6$ surface produce bountiful reactive oxygen species for mineralizing VOCs and sweeping bacteria. Enriched with •O$_2$ and •OH, a 15 cm*5 cm Na-Bi$_2$WO$_6$ mesh can completely degrade 30 ppm toluene in 0.45 dm^3 reactor in 1 hour without producing any toxic intermediates like benzene, and its efficacy only decayed by 4% after a continuous 14-hour run. A cup-shaped air purifier was assembled with the Na-Bi$_2$WO$_6$ mesh, enabling the rapid elimination of 1 ppm toluene, 2 ppm formaldehyde, and bacteria within a 120 dm^3 test space.

1. Introduction

Volatile organic compounds (VOCs) are a class of air pollutants with boiling points ranging from 50 °C to 260 °C under ambient conditions [1]. VOCs in atmosphere not only damage the ozone layer in the atmosphere but also react with NO$_x$ and SO$_x$ to form photochemical smog [2,3]. Additionally, VOCs are toxic and carcinogenic[4]. Toluene, benzene, formaldehyde, xylene and methylene chloride are representatives, with the first three being well known as they are frequently reported pollutants. Short-term and single exposure to polluted air can lead to immediate health effects such as dizziness, fatigue, weakness, and cough [5,6], which are generally temporary and treatable. Once the pollutants are identified, removing the sources or keeping away from the environment is workable to eliminate the symptoms. Nevertheless, long-term and unaware exposure to VOCs sometimes can cause irreversible harm to humans. When the symptoms show up, the situation may have reached a serious stage. Some respiratory diseases, heart disease and cancer, can be severely debilitating or fatal.

In terms of an indoor air pollution in family life, the main sources of VOCs include building materials, furnishings, newly installed flooring, upholstery or carpet, as well as printers, household cleaning products. With the outbreak of COVID-19 and the epidemic of its variants until now, the demand for efficient air cleaners in residential educational and work settings is climbing, as more and more people are recognizing the significance of maintaining high Indoor Air Quality (IAQ). Removing VOCs and ventilating with fresh outdoor air can enhance the IAQ. However, during winter, closed window and burning furnace will aggravate the VOCs-triggered air pollution due to inadequate ventilation. Therefore, people turn to air purifiers to improve the IAQ and abate the health risk. Common VOCs removal methods involved in air purifier contain physical absorption and chemical oxidation, which remove pollutants from air by either recovery or destruction[7]. When dealing with high concentration or long-term situation, the effectiveness of physical absorption methods such as using active carbon is limited once the absorption capacity is fulfilled. Periodic cleaning and filter replacement are necessary to ensure the proper functioning, leading to increased costs. In contrast, oxidation through catalysis with photocatalysts prevails over physical absorption in breaking down the

---

hazardous VOCs into CO_2 and H_2O. Apart from that, these catalysts loaded with reactive oxygen species (ROS) can facilitate disinfection. Since O_3 is an undesired by product generated under UV lights with wavelength between 100 and 240 nm, air purifiers equipped with visible-light-driven photocatalysts are more promising and popular. These devices do not produce O_3 during operation, making them a preferred choice. Bi_2WO_6, as one of the typical Aurivillius oxides, can fully harvest the UV, visible, and IR light[8], which is widely applicable in photocatalysis such as removing organic pollutants from water[9,10], and converting CO_2 into valuable hydrocarbons[11]. Concerning Bi_2WO_6-based photocatalysts for toluene degradation, heterojunctions are the most conventional, including $BiOI/Bi_2WO_6/ACF$[12], $BiO-Cl/Bi_2WO_6$[13], $Ag/AgCl/Bi_2WO_6$[14], WO_3/Bi_2WO_6[15], In_2S_3/Bi_2WO_6[16], and $CuInS_2/Bi_2WO_6$[17]. Besides that, doping Bi_2WO_6 with metal ions and non-metal ions as diverse as Ce[18], Yb [19], Fe[20], Cu[21], P[22], S[23], F[24], I[25] have been explored to improve the activity of Bi_2WO_6 for eliminating organic pollutants. However, few studies concern the alkali metal ions and their influence on Bi_2WO_6 morphology and properties. Actually, alkali metal ions (Li^+, Na^+, K^+) are known for their intercalation effect applied to separate the stacking of sheet-shaped materials[26]. Bi_2WO_6 crystals generally appear as nanoflakes due to the alternative stacking of [BiO]-$^+$–$[WO_4]^{2-}$–$[BiO]^+$ with oxygen atoms shared between layers[27], which indicates that oxygen vacancies (OVs) will be created when the space among building block layers are expanded by the implanted heteroatoms.

Illuminated by above findings, in this study, Bi_2WO_6 nanoflakes tailored by Li^+, Na^+, K^+ were grown on a pliable W mesh through a self-sacrifice template approach. A comparative analysis reveals that the implantation of Na^+ boosts the supreme laminar splitting of Bi_2WO_6 crystal, resulting in the generation of ultrathin Bi_2WO_6 nanosheets. The impact of K^+ is inferior to that of Na^+, while Li^+ proves ineffective due to its small size. Abundant OVs can be generated as result of the laminar splitting, accompanied with shorted pathway for carrier transferring. Furthermore, the OVs serve as electron capture centers, thereby prolonging the carrier lifetime[28,29]. DFT results manifest that the Na^+ insertion reinforces the adsorption of toluene, H_2O, and O_2 on Bi_2WO_6, favoring the activation of toluene skeleton and creating more hydroxyl radicals ($\bullet OH$) and superoxide radicals ($\bullet O_2$). The degradation of toluene follows a $\bullet OH$-governing evolution pathway. The direct graft of -OH on benzene ring of toluene activates the carbon skeleton, making it vulnerable to ROS. Efficient and rapid mineralization is achieved without the production of hazardous benzene during the evolution process. Moreover, the performance of $Na-Bi_2WO_6$ against bacteria under visible lights is also notable, validating its advance in photocatalytic disinfection.

Taken as a whole, large surface area on the outside, countless OVs and prompt electron transfer within, as well as the structural integrity, these natures of $Na-Bi_2WO_6$ make it feasible and available to manufacture a portable all-in-one air purifier for getting rid of VOCs and bacteria.

2. Experimental section

2.1. Chemicals and materials

Bismuth nitrate pentahydrate ($Bi(NO_3)_3 \cdot 5 H_2O$), lithium nitrate ($LiNO_3$), sodium nitrate ($NaNO_3$), and potassium nitrate (KNO_3) were purchased from the Guoyao Co. Ltd. China. Nitric acid (HNO_3, 69 wt%) and hydrogen Peroxide (H_2O_2, 30 wt%) were purchased from the Xilong Science Co. Ltd. Tungsten (W, 99.8% in purity, pore-size : 0.2 mm, thickness: 0.12 mm, porosity:38%) mesh was purchased from An Ping Jiangxin wire mesh products Co. Ltd, which was cleaned to remove the surface grease with acetone, ethanol and water in sequence. LB-Broth were purchased from the Shanghai Aladdin Biochemical Technology Co., Ltd. *Staphylococcus aureus* [CMCC (B) 26003] and *Escherichia coli*

[CMCC (B) 44102] were purchased from the Beijing Sanyao Technology Co., Ltd.

2.2. Fabrication of alkali ions-Bi_2WO_6 through a self-sacrifice template strategy

Tungsten (W) mesh was cut into the size of 15 cm*5 cm as substrate. Before bearing Bi_2WO_6, the W mesh was ultrasonicated in acetone and ethanol for 15 min in sequence to remove grease and dust on the W mesh surface. In a typical synthesis process, a clean W mesh was placed in a 50 mL of deionized water, then 0.9 mL HNO_3 and 0.9 mL H_2O_2 were added in sequence to oxidize W^0 to H_2WO_4 for serving as W precursor of Bi_2WO_6. 30 min later, the W mesh was taken out temporarily, 1 mmol Bi $(NO_3)_3 \cdot 5 H_2O$ and 2.5 mmol $NaNO_3$ (or 2.5 mmol $LiNO_3$, 2.5 mmol KNO_3) were dissolved in the H_2WO_4 solution. Then the mixture was magnetically stirred for 30 min. After that, the obtained suspension and W mesh were transferred into a 50 mL of Teflon-lined autoclave for 24 h heat treatment at 160 °C. After the reaction was over, alkali ions engineered Bi_2WO_6 nanoflakes cover every W wire of the mesh. Pristine Bi_2WO_6 was prepared the same way without alkalis ions. For better comparison, the influence of hydrothermal duration (12 h, 24 h, and 36 h) on the pristine Bi_2WO_6 was studied. The corresponding SEM images, XRD patterns, and their performance in photocatalytic degrading toluene are provided in Fig. S1. As shown, the thickness of Bi_2WO_6-12 h, Bi_2WO_6-24 h, and Bi_2WO_6-36 h is 5.5 nm, 7.9 nm, and 18.9 nm, respectively. The photocatalytic performance in degrading toluene using these pristine Bi_2WO_6 catalysts was determined. As shown in Fig. S1e and S1f, Bi_2WO_6-24 h has the best photocatalytic activity. Therefore, Bi_2WO_6-24 h was used for the blank experiment.

W mesh before hydrothermal treatment and $Na-Bi_2WO_6$/W mesh were weighed using a photoelectric analytical balance, and their weights were labeled as w_0 and w_1. For a 15 cm*5 cm W mesh, w_0 was 2120 mg, and w_1 was 2180 mg. The loading amount of $Na-Bi_2WO_6$ calculated by subtracting w_0 from w_1 was 60 mg.

2.3. Characterization

Names and types of the precision instruments like SEM, AFM, AC-TEM, TEM, XPS, UV–vis spectrophotometer, employed for characterizing the morphology, crystal structure, and valance state and chemical environment of the catalysts, assessing light absorption, photoelectric conversion capacity, ect. are provided in Supporting Information (SI) file.

2.4. Photocatalytic degradation of toluene and details of antibacterial experiments

A self-developed reactor for photocatalytic oxidation of VOCs was utilized to study the catalytic oxidation reaction of toluene at room temperature (Fig. S2). Briefly, the toluene concentration was set as 30 ppm, a xenon lamp was employed to provide solar illumination, and equipped with a 420 nm cut-off filter to prevent ultraviolet rays. The residual toluene concentration and CO_2 yield were determined using the gas chromatography (GC), and the intermediate generated during the degradation process were dissolved in methanol for identification using GC-MS spectrometry. The standard curves of gas chromatographic peak area versus toluene concentration are shown in Fig. S3.

The antibacterial activity of $Na-Bi_2WO_6$ was evaluated using the typical pathogenic bacteria *S. aureus* and *E. coli* as targets. In a typical process, the purchased original cultures were incubated in 300 mL of liquid medium at 30 °C for 24 h and cryopreserved for subsequent use. Subsequently, 3 mL of bacterial solution and 10 mg catalyst peeled from W mesh were added in the liquid medium under stirring to create a homogeneous mixture. To assess the photocatalytic performance of Na-Bi_2WO_6, the experiments were divided into four groups. Three of them were control groups including one was naturally cultured without

catalyst and light, labeled as blank; another group was added with catalyst without illumination; and the third group was illuminated by lights without Na-Bi_2WO_6. The light source is the xenon lamp, irradiation time is 15 min. Afterwards, every medium was sampled (50 μL) and incubated at 30 °C for 20 h. The antimicrobial activity of the catalyst was evaluated by counting the number of colonies of *E. coli* and *S. aureus* grown on nutrient agar plates.

3. Results and discussion

3.1. Structural and morphological variations in Bi_2WO_6 endowed by Li^+, Na^+, and K^+

Digital pictures in Fig. 1a real that the W mesh color changes from the original black to dark gray after the hydrothermal reaction. The pristine Bi_2WO_6 nanoflakes (Fig. 1b and f) are approximately 7.782 nm thick, they are regularly interlaced to create an interface with numerous pores, corners and edges. Each W wire is wrapped by the Bi_2WO_6 layer, constructing a practical three-dimensional self-supporting catalyst, exhibited as Fig. S4a. As for Li-Bi_2WO_6 (Fig. 1c and g), there is notable change in thickness, the Bi_2WO_6 nanoflake is around 5.605 nm thick, and its surface appears rumpled with small sheets (Fig. S4c), totally different from the smooth surface of pristine Bi_2WO_6 (Fig. S4b), demonstrating a tendency of crystal splitting. Compared with the Li^+ ions, K^+ and Na^+ exhibit greater potency. Na^+ (Fig. 1d) and K^+ (Fig. 1e) fuel a novel and supreme layered splitting of Bi_2WO_6. As shown, a high density of ultrathin Bi_2WO_6 nanoflakes with a regular arrangement outstretch from the core knot, which is typical crystal splitting. The thickness of Na-Bi_2WO_6 is about 3.848 nm (Fig. 1h), and that of K-Bi_2WO_6 is 4.022 nm (Fig. 1i), about half of the pristine Bi_2WO_6. It looks like that the stacking of $[BiO]^+–[WO_4]^{2}–[BiO]^+$ layers is inserted with Na^+ or K^+ ions, leading to the halving of the Bi_2WO_6 nanoflakes.
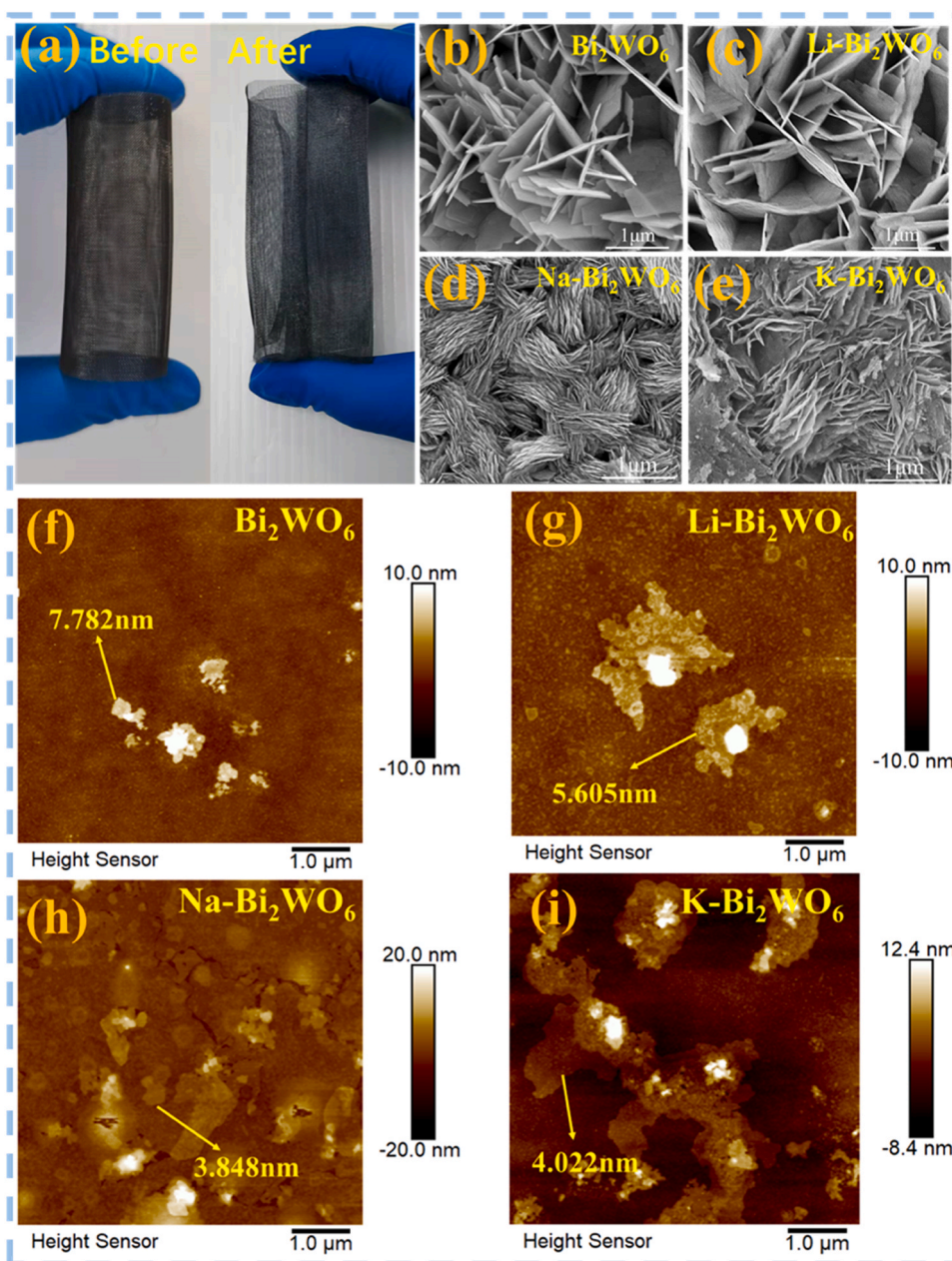
Fig. 1. (a) W mesh before and after hydrothermal reaction; SEM image of (b) Bi_2WO_6, (c) Li-Bi_2WO_6, (d) Na-Bi_2WO_6, (e) K -Bi_2WO_6. AFM image of (f) Bi_2WO_6, (g) Li-Bi_2WO_6, (h) Na-Bi_2WO_6, (i) K-Bi_2WO_6.

Moreover, the ion radius of K^+ is 138 pm, larger than Na^+(102 pm), K^+ ions create the over-splitting of Bi_2WO_6. As Fig. 1e exhibits, there appear to be melted regions, which can be attributed to the broken stacking of Bi_2WO_6 nanoflakes.

The elemental map of Na^+ in Fig. S5 evidences its uniform distribution in Bi_2WO_6. The specific position of Na^+ in the crystal structure of Bi_2WO_6 was further characterized using AC-TEM. Fig. 2a demonstrates the typical HAADF-STEM image of Na-Bi_2WO_6, with the magnified zone marked by red circle revealing the specific distribution of Na in Bi_2WO_6. Fig. 2b exhibits the distribution of colored atoms: purple for Na, orange for W, and cyan for Bi, they are mixed together. In the uncolored HAADF-STEM image, Na, W, and Bi show a bright-dark interlaced pattern because the atomic numbers of Bi (83) and W (74) are much higher than Na (11). Consequently, the positions of Bi and W atoms appear bright while those of Na atoms appear dark.

Gatan Microscopy Suite was utilized to refine Fig. 2a and magnified it to obtain a clear picture illustrating the positions of Na, W, and Bi. Based on the results of STEM-EDS (Fig. 2b and Fig. S5), the approximate position of Na atom was determined (Fig. 2c), and the dark field was characterized by electron energy loss spectroscopy (EELS). As shown in Fig. 2d, the intensity peak of Na-*K* appears at 1080–1086 eV[30], and Na atom is sandwiched between $[BiO]^+$ and $[WO_4]^{2-}$ layers.

The thinner and denser Bi_2WO_6 nanoflakes provide an open interface with numerous active sites for the uptake of gaseous molecules. Additionally, the thinned layer will shorten the carrier transport distance and accelerate the electron transfer along Bi_2WO_6, contributing to promoting the photocatalytic activity[31]. To the best of our knowledge, it is the first study to reveal the effect of Li^+, Na^+, and K^+ on the crystal splitting of Bi_2WO_6.

The XRD patterns (Fig. 3a) of pristine Bi_2WO_6, Li-Bi_2WO_6, Na-Bi_2WO_6, and K-Bi_2WO_6 demonstrate variations in the Bi_2WO_6 crystallinity due to the intercalation of alkalis ions. All the candidates have identical diffraction peaks centered at 28.3 °, 32.8 °, 47.1 °, and 56.0 °, indexed to the (131), (002), (202), and (133) crystal planes of orthorhombic Bi_2WO_6 (PDF#79–2381), respectively[32]. Except the specific peaks of W substrate sited at 40 °, 73 °, no other impurity peaks were detected. Notably, compared with the pristine Bi_2WO_6, alkalis-Bi_2WO_6 candidates show broadened diffraction peaks, indicating the crystallinity of Bi_2WO_6 is declined owing to the implantation of Li^+, Na^+, and K^+ [33]. As an illustration, the magnified peak corresponding to (002) plane centered at 32.8 ° (Fig. 3b) negatively shifts toward a lower 2θ value, indicating the expanded lattice space of (002) plane[34]. As the ion radius rises in the order of Li^+-76 pm <Na^+-102 pm <K^+-138 pm, K^+ induces the most prominent deviation, followed by Na-Bi_2WO_6, with Li-Bi_2WO_6 exhibiting the least deviation.

TEM images in Fig. S6a-d shed light on illustrating the inner structural characteristics of Bi_2WO_6 and alkalis-Bi_2WO_6. Both the original Bi_2WO_6 and alkalis-Bi_2WO_6 consist of nanoflakes, which is coincide with the SEM results. Moreover, the elemental maps of Na, K (Fig. 4a, b) evidence their uniform distribution in Bi_2WO_6. Li mapping was not collected because the weight of Li is too low to be recognized by the analyzer equipped on TEM (Fig. S6f).

The HRTEM images demonstrate the lattice fringe corresponding to (002) plane of Bi_2WO_6 varies with the presence of Li^+, Na^+, and K^+, which is 0.273 nm for Bi_2WO_6, 0.281 nm for Li-Bi_2WO_6, 0.283 nm for Na-Bi_2WO_6, and 0.284 nm of K-Bi_2WO_6 (Fig. 4c-f). The expanded lattice spacing is related to the intercalation of alkali cations in Bi_2WO_6. The larger the cation, the wider the lattice fringes. Moreover, those areas
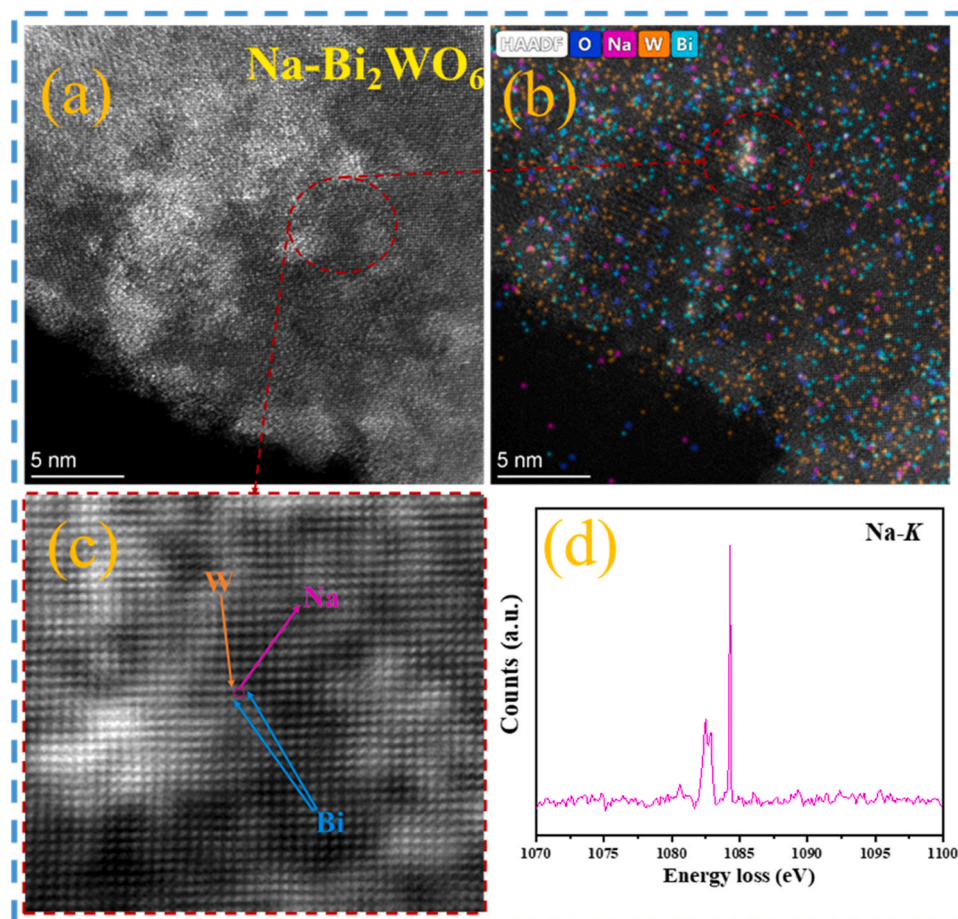
Fig. 2. (a) HAADF-STEM image of Na-Bi_2WO_6. (b) STEM-EDS mapping images of Na-Bi_2WO_6. (c) HAADF-STEM images of Na-Bi_2WO_6 refined using Gatan Microscopy Suite. (d) STEM-EELS spectrum of Na-Bi_2WO_6.
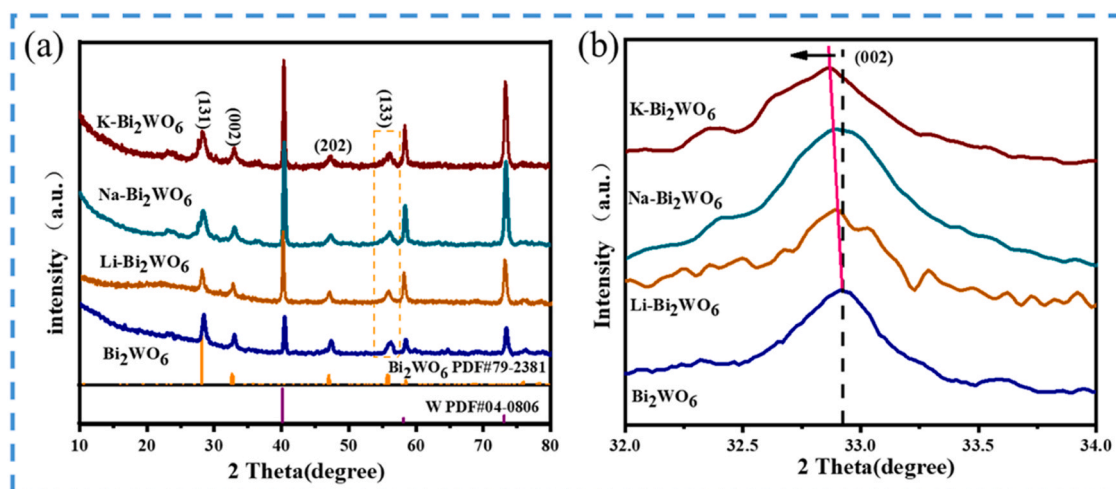
Fig. 3. (a) XRD patterns of Bi$_2$WO$_6$, Li-Bi$_2$WO$_6$, Na-Bi$_2$WO$_6$, and K-Bi$_2$WO$_6$, (b) enlarged part from 32 ° to 34 °.

marked by yellow circles in Fig. 4d, 4e, f exhibit lattice disorder and dislocation, validating the presence of coordinatively unsaturated metal atoms inspired by the vacancies[35,36]. Low-temperature EPR analysis was carried out to identify the OVs which signal is centered at g=2.003 [37]. Fig. 4g shows that the pristine Bi$_2$WO$_6$ nanoflakes don't have OVs, but alkalis cations in Bi$_2$WO$_6$ crystal give rise to many defects, and Na$^+$ ranks the first.

Since defects affect the elemental valence state in catalysts, XPS analysis was conducted to identify the influence of Li$^+$, Na$^+$, and K$^+$. The survey XPS scans of Bi$_2$WO$_6$ and alkalis-Bi$_2$WO$_6$ catalysts are presented in Fig. 4h and Fig. S7. Although the signals of Li, Na, K are tiny due to their low contents, the high-resolution (HR) XPS spectra of Li 1 s[38], Na 1 s[39], and K 2p[40] in Fig. S7a-c confirm the presence of Li$^+$, Na$^+$ and K$^+$, respectively.

Fig. 5a depicts that the binding energies of W 4 f$_{7/2}$ and W 4 f$_{5/2}$ are 35.5 eV and 37.6 eV in pristine Bi$_2$WO$_6$[41,42], which increase by 0.4 eV on account of the alkalis. As for Bi 4 f$_{7/2}$ and Bi 4 f$_{5/2}$ (Fig. 5b) initially located at 159.1 eV and 164.4 eV, respectively, a 0.4 eV of chemical shift is rendered by Li$^+$, 0.9 eV by Na$^+$ and 0.7 eV by K$^+$. The positive shifts in binding energies indicate that the electrons around W^{6+} and Bi^{3+} electrons migrate to the electron-deficient sites[43]. In Fig. 5c, the O 1 s from the original Bi$_2$WO$_6$ are deconvoluted into three peaks, 530.25 eV, 531.76 eV, and 533.45 eV, corresponding to lattice oxygen (O$_{latt}$), adsorbed oxygen (O$_{ads}$), and surface hydroxyl oxygen (O$_{-OH}$) from the adsorbed water, respectively[44,45]. With alkalis cations implanted, the contents of O$_{latt}$ drop significantly, decreased from 71.78% in Bi$_2$WO$_6$ to 63.57% in Li-Bi$_2$WO$_6$, 47.32% in K-Bi$_2$WO$_6$, 38.04% in Na-Bi$_2$WO$_6$, accompanied by a growth of O$_{ads}$.

Among all the Bi$_2$WO$_6$ candidates, the O1s spectra of Na-Bi$_2$WO$_6$ exhibits the highest percentages of O$_{ads}$ (37.84%), and O$_{-OH}$ (24.12%), indicating that Na$^+$ ions contribute significantly to the creation of OVs because surface vacancies are prone to adsorb gaseous O$_2$ and H$_2$O. These outstanding features will enable Na-Bi$_2$WO$_6$ prominent in producing •O$_2^-$ and •OH[46]. As the EPR spectra of OVs (Fig. 4g) and the XPS spectra in Fig. 5 verify, surface Bi atoms are coordinatively unsaturated and therefore the [BiO]$^+$ layers are enriched with active sites. In the light of Bi$_2$WO$_6$ crystal construction, under irradiation, holes will be generated on the [BiO]$^+$ layers, and electrons will gather in the middle [WO$_4$]$^{2-}$ layer[27].

3.2. Optical and photochemical property of Bi$_2$WO$_6$ and alkalis Bi$_2$WO$_6$

The light-harvesting capacity of Bi$_2$WO$_6$ and alkalis-Bi$_2$WO$_6$ are depicted in Fig. 6a. After incorporating Li$^+$, Na$^+$, and K$^+$ into Bi$_2$WO$_6$, the absorption edge of alkalis-Bi$_2$WO$_6$ shifts towards longer wavelengths

and the absorption intensity increases. Band gap energies were estimated using the Kubelka-Munk function, as listed below.

$$(\alpha h\nu)^2 = A(h\nu - E_g)^n$$

In this equation, α is the absorption coefficient, h is Planck's constant, ν is the light frequency, and A is the proportionality constant. The value of n depends on the semiconductor type, for Bi$_2$WO$_6$, n is equal to 1[47]. The calculated band gaps of Bi$_2$WO$_6$ and Li-Bi$_2$WO$_6$, Na-Bi$_2$WO$_6$, K-Bi$_2$WO$_6$ are 2.92 eV, 2.80 eV, 2.71 eV, and 2.83 eV, respectively (Fig. 6b). OVs in Bi$_2$WO$_3$ create donor levels positioned between the conduction band and valence band, which can favor the promoted uptake of visible lights and contribute to the photocatalytic reaction [48–50].

It's known that plenty of active photogenerated carriers with long lifetime are essential for a high-performance catalyst. Transient photocurrents (Fig. 7a) recorded on Bi$_2$WO$_6$ and alkalis-Bi$_2$WO$_6$ meshes rank the impact from Li$^+$, Na$^+$, and K$^+$. The highest current on Na-Bi$_2$WO$_6$ suggests that Na$^+$ performs best for curbing the recombination of the electron-hole pairs, which is 3.6 times that on Bi$_2$WO$_6$. SPV measurements gives the potential of a semiconductor surface when generating electron-hole pairs under irradiation. The increased SPV illustrates that a greater number of photogenerated carriers deep within the semiconductor can diffuse through the bulk and finally reach the surface without combination[51]. As shown in Fig. 7b, the SPV ranks in the order of Na-Bi$_2$WO$_6$>K-Bi$_2$WO$_6$>Li-Bi$_2$WO$_6$>Bi$_2$WO$_6$, evidencing that Li$^+$, Na$^+$, and K$^+$ ions facilitate the effective separation of photogenerated electron-hole pairs, and Na$^+$ ions provide a fast transfer channel for carrier diffusing and transferring[52]. The SPV recorded on Na-Bi$_2$WO$_6$ approaches 1.8 V, almost 4 times that on the pristine Bi$_2$WO$_6$.

Moreover, the lowest PL emission spectrum is delivered by Na-Bi$_2$WO$_6$ (Fig. 7c), suggesting the separation probability of hole-electrons is the highest. Fig. 7d and Table S1 summarize the average lifetimes of the photoelectrons on Bi$_2$WO$_6$, Li-Bi$_2$WO$_6$, Na-Bi$_2$WO$_6$, and K-Bi$_2$WO$_6$, which are 1.12 ns, 1.20 ns, 1.78 ns, and 1.48 ns, respectively. The results in Fig. 7 clarify that implanting alkalis ions like Na$^+$ in Bi$_2$WO$_6$ effectively extend the lifetime of carriers, and the long-lived photoinduced carriers will boost the generation of more active species, leading to the exceptional photocatalytic efficiency[53,54].

3.3. Photocatalytic degradation of toluene on Bi$_2$WO$_6$ and alkalis-Bi$_2$WO$_6$ candidates

Photocatalytic degradation of toluene at the same concentration under visible lights over Bi$_2$WO$_6$, Li-Bi$_2$WO$_6$, Na-Bi$_2$WO$_6$, and K-Bi$_2$WO$_6$
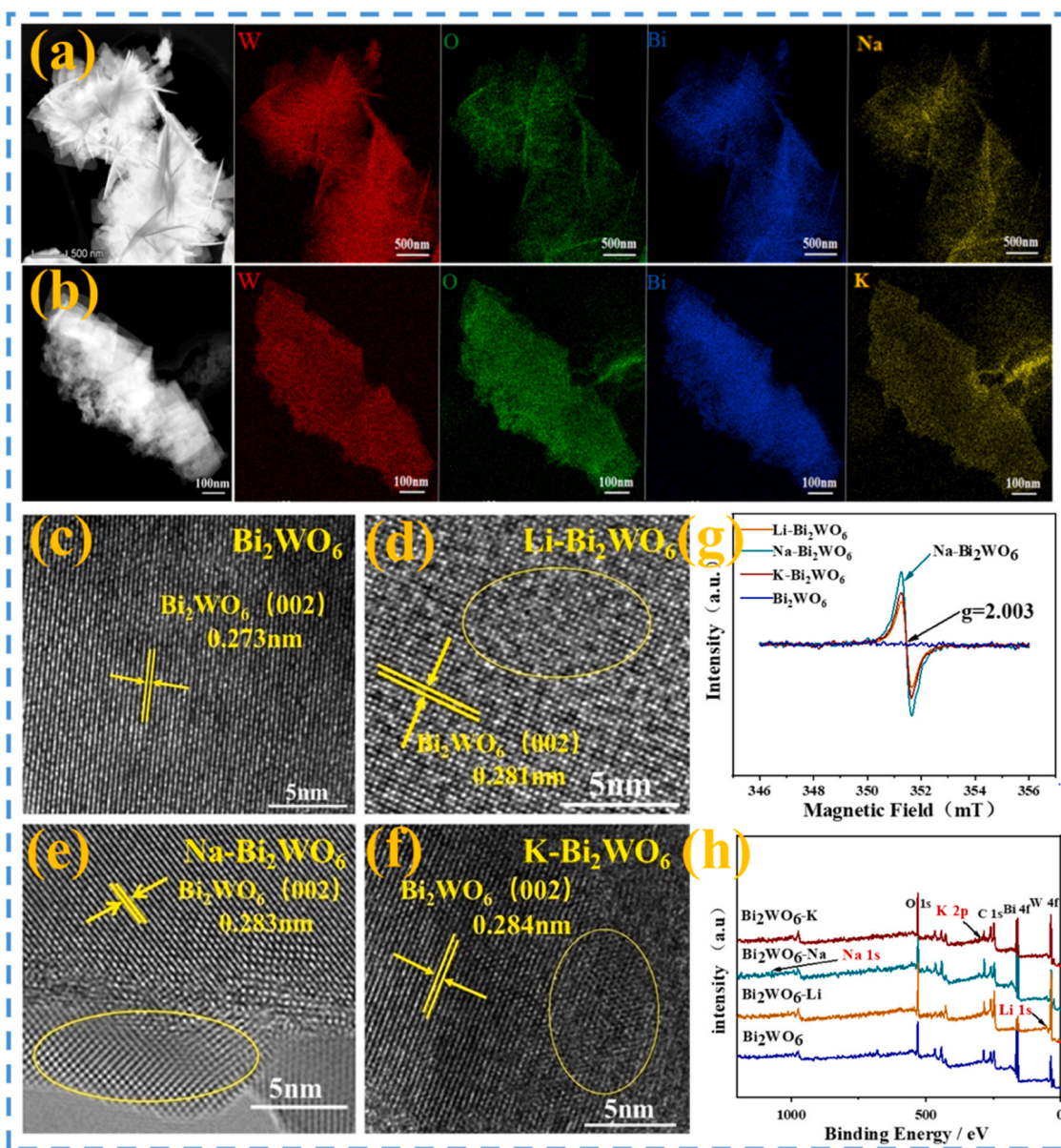
Fig. 4. EDS mapping images of (a) Na-Bi_2WO_6 and (b) K-Bi_2WO_6. HRTEM images of (c) Bi_2WO_6; (d) Li-Bi_2WO_6, (e) Na-Bi_2WO_6, and (f) K-Bi_2WO_6. (g) EPR spectra of OVs and Bi_2WO_6, Li-Bi_2WO_6, Na-Bi_2WO_6, and K-Bi_2WO_6. (h) The overall XPS spectra of all catalysts.

was carried out to evaluate the impact of alkalis cations. Actually, before the comparative study, three Na-Bi_2WO_6 meshes were synthesized under different amounts of $NaNO_3$ containing 1.25 mmol, 2.5 mmol, and 3.75 mmol, and their photocatalytic properties for toluene degradation under identical conditions were studied. As depicted in Fig. S8, Na-Bi_2WO_6 with 2.5 mmol exhibits the best photocatalytic performance, completely mineralizing 30 ppm toluene in CO_2 and H_2O. Therefore, the "2.5 mmol" was selected as the optimal precursor amount of Na^+, K^+, Li^+. In Fig. 8a and b, the removal percentage of toluene on the pristine Bi_2WO_6 within 90 min is 52.3%, while those on Bi_2WO_6 engineered with Li^+, Na^+, and K^+ are sequenced as Li-Bi_2WO_6 (79.2%) <K-Bi_2WO_6 (85.1%) <Na-Bi_2WO_6 (100%). Na-Bi_2WO_6 exhibits the best performance, achieving complete removal of toluene, a 47.7% enhancement over pristine Bi_2WO_6. Nevertheless, only using declined toluene concentration to assess the catalytic performance of alkalis-Bi_2WO_6 is insufficient, as several intermediates (benzene, phenol, benzyl alcohol, benzaldehyde and benzoic acid) are generated when the degradation of toluene proceeds[36,55].

Therefore, CO_2 yield was determined, based on which the

mineralization degree of toluene was calculated to evaluate the capability that Bi_2WO_6 and alkalis-Bi_2WO_6 directly break down the toluene molecules. As shown, 23.5% of 30 ppm toluene is oxidized in CO_2 and H_2O with the pristine Bi_2WO_6. When alkalis cations are involved, the mineralization degree of toluene is significantly promoted. The highest one on Na-Bi_2WO_6 is 96.6%, which is 4.11 times that on the pristine Bi_2WO_6, climbed by 73.1% in the same duration. The 100% of removal efficiency and 96.6% of mineralization degree mean that Na-Bi_2WO_6 can effectively eliminate toluene without producing any toxic intermediates, which is essential and critical for manufacturing a safe photocatalytic air cleaner. The performance of different sizes of Na-Bi_2WO_6/W mesh for toluene degradation was also studied. As Fig. S9 shown, with enlarged Na-Bi_2WO_6/W mesh to 15 cm*10 cm, the efficiency of toluene degradation and photocatalytic disinfection are doubled.

Taking the optimal Na-Bi_2WO_6 as catalyst, toluene with increased initial concentrations of 30 ppm, 64 ppm, 96 ppm, 122 ppm, and 155 ppm was decomposed under visible lights. As Fig. 8c exhibits, the removal percentage goes down from 100% to 60.1% with the toluene concentration increased from 30 ppm to 155 ppm. The corresponding
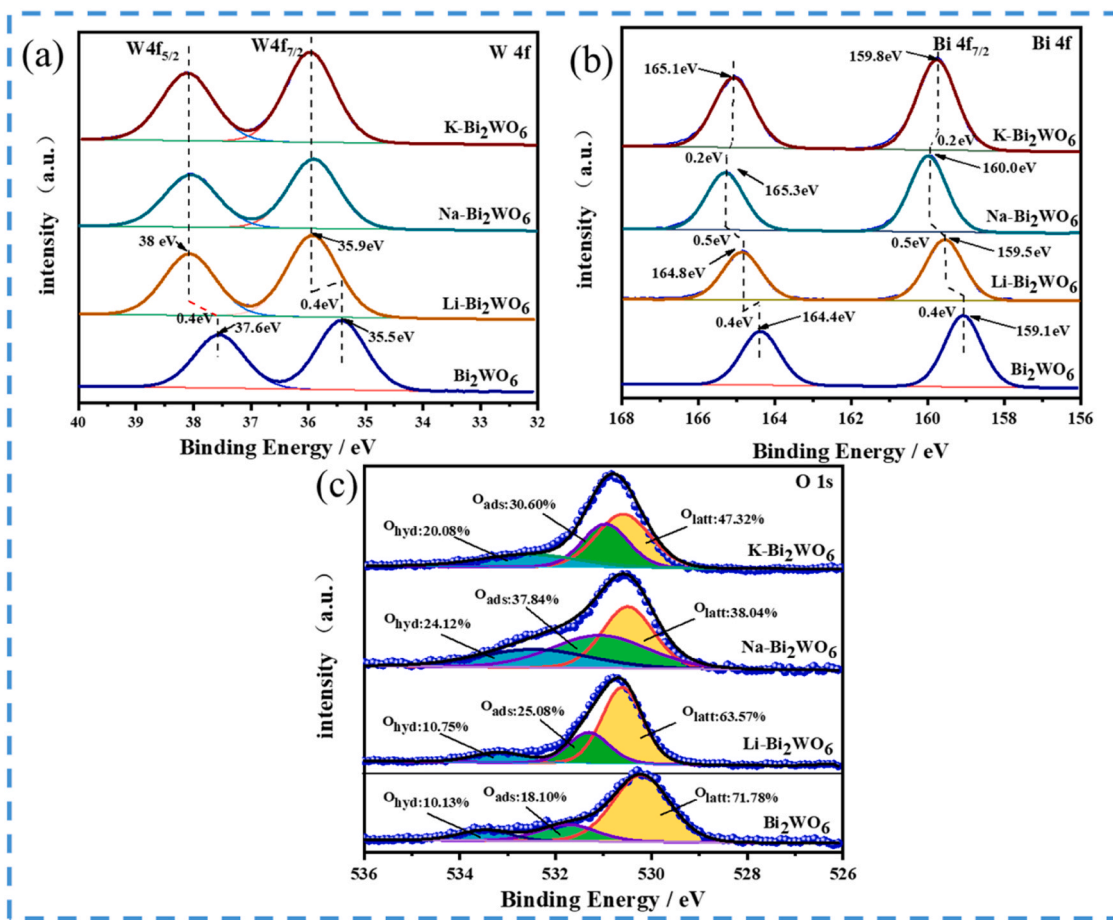
Fig. 5. High-resolution XPS spectra: (a) W 4 f, (b) Bi 4 f and (c) O 1 s of Bi_2WO_6, $Li-Bi_2WO_6$, $Na-Bi_2WO_6$, and $K-Bi_2WO_6$.
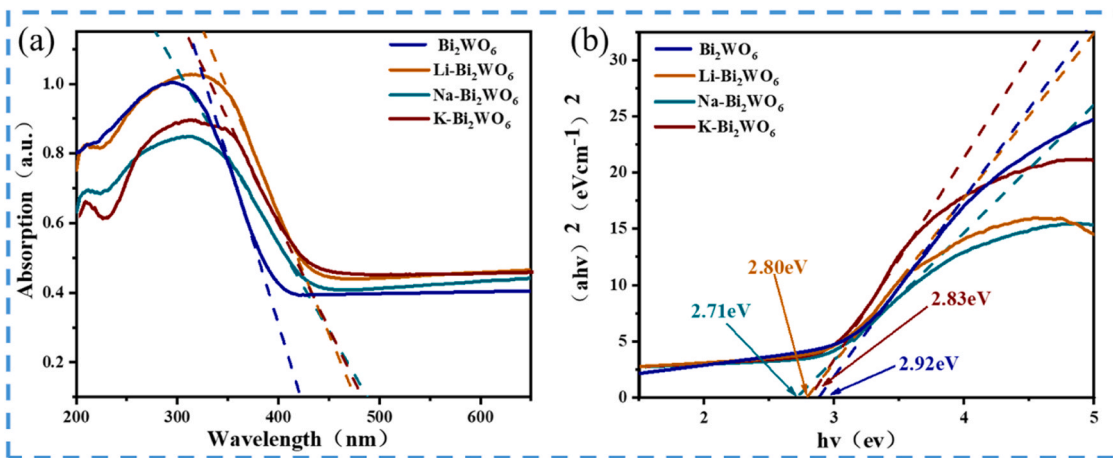
Fig. 6. (a) UV–vis diffuse reflectance spectra of Bi_2WO_6, $Li-Bi_2WO_6$, $Na-Bi_2WO_6$, and $K-Bi_2WO_6$. (b) the corresponding plots of $[\alpha h\nu]^2$ vs photon energy.

kinetic analysis (Fig. 8d) depicts that the oxidation of toluene follows a quasi-first order model, clarifying this is a typical gas-solid reaction, the degradation takes places on the catalyst surface and its reaction rate is determined by the active radicals[56].

N_2 adsorption-desorption isotherms and pore size distributions of the pristine Bi_2WO_6, $Li-Bi_2WO_6$, $Na-Bi_2WO_6$, and $K-Bi_2WO_6$ catalysts were investigated, with results shown in Fig. S10. All of them exhibit similar typical IV isotherms with H3-type hysteresis loops, demonstrating their mesoporous structures resulting from the stacking of nanoflakes. Specific surface area, pore volume, and pore diameter were calculated according to the BET and BJH models, and are summarized in Table S2. Among them, $Na-Bi_2WO_6$ has the largest BET surface area (66.5 $m^2 \cdot g^{-1}$), followed by $K-Bi_2WO_6$ (55.5 $m^2 \cdot g^{-1}$), $Li-Bi_2WO_6$ (42.7 $m^2 \cdot g^{-1}$), and Bi_2WO_6 (28.6 $m^2 \cdot g^{-1}$) in sequence. Generally, a large surface area will supply more adsorption sites and active sites, which is one of the determinants for gas-solid reactions.
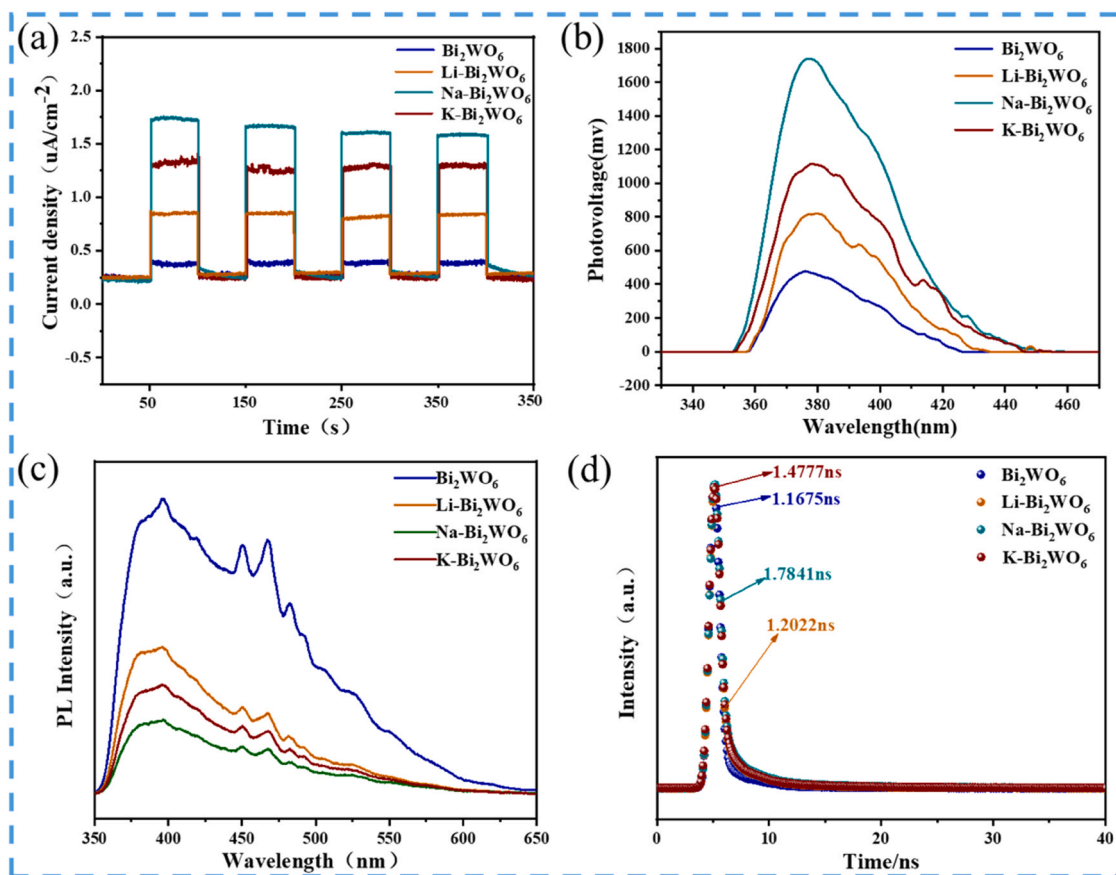
Fig. 7. (a) Photocurrent responses (b) Surface photovoltage (c) PL spectra and (d) time-resolved transient PL decay curve of Bi_2WO_6, Li-Bi_2WO_6, Na-Bi_2WO_6, and K-Bi_2WO_6.

3.4. Degradation behavior of toluene on Na-Bi₂WO₆ and involved mechanism

OVs can trigger the generation of electron-rich confined centers, and regulate the band structure for curbing the recombination of hole-electron pairs. The quantity of OVs is tied with the yield of ROS that is paramount in oxidizing the organic chemicals. Demonstrated as Fig. 9a and b, EPR signals of $\bullet O_2^-$ and $\bullet OH$ recorded on the catalysts depict that alkalis-Bi_2WO_6 catalysts supply many more $\bullet O_2^-$ and $\bullet OH$ than pristine Bi_2WO_6. The quantitative analysis of these radicals was also carried out, related results are listed in Table S3. The concentrations of $\bullet O_2^-$ on Bi_2WO_6, Li-Bi_2WO_6, Na-Bi_2WO_6, and K-Bi_2WO_6 are 5.157×10^{-6} mol/L, 8.699×10^{-6} mol/L, 1.535×10^{-5} mol/L, and 1.145×10^{-5} mol/L in sequence. The concentrations of $\bullet OH$ on Bi_2WO_6, Na-Bi_2WO_6, and K-Bi_2WO_6 catalysts are 7.083×10^{-5} mol/L, 9.621×10^{-5} mol/L, 1.635×10^{-4} mol/L, and 1.206×10^{-4} mol/L, respectively. Particularly, the rises in $\bullet O_2^-$ and $\bullet OH$ yields are more remarkable on Na-Bi_2WO_6, which surpasses all the other catalysts. It turns out that Na-Bi_2WO_6 enriched with OVs can adsorb more H_2O and O_2 molecules from the atmosphere and convert them in oxidant radicals, eventually speeding up the mineralization process of toluene.

In the following section, DFT calculation is applied to expound the detailed absorption behaviors of toluene (C_7H_8), H_2O, and O_2 on Bi_2WO_6 and alkalis-Bi_2WO_6 to reveal the involved photocatalytic mechanism.

The adsorption and activation of target C_7H_8 on catalytic interface is the crucial step before the subsequent degradation. Fig. 10 shows the most stable configurations displaying the adsorption of C_7H_8, O_2, and H_2O molecules on Bi_2WO_6 and Na-Bi_2WO_6. Those of Li-Bi_2WO_6 and K-Bi_2WO_6 are supplemented in Fig. S11. Compared with pristine Bi_2WO_6, reinforced adsorption toward C_7H_8, O_2, and H_2O are achieved by Li-

Bi_2WO_6, Na-Bi_2WO_6 and K-Bi_2WO_6. Specifically, for Na-Bi_2WO_6, the adsorption energy of C_7H_8 molecule is -0.99 eV, which is 3 times that on the pristine Bi_2WO_6. In addition, comparison of the electron localization function (ELF) diagrams of C_7H_8 reveals that there are more orange regions between Na-Bi_2WO_6 and C_7H_8, which means that C_7H_8 molecule is noticeably activated by the electrons from Na-Bi_2WO_6 because electron streams and affirm bonds are formed between them. The strengthened anchorage for O_2 and H_2O is observable on $O_2@Na$-Bi_2WO_6 and $H_2O@Na$-Bi_2WO_6. Above results elucidate why Na-Bi_2WO_6 is capable of supplying more $\bullet O_2^-$ and $\bullet OH$.

The contact angles of water on Bi_2WO_6, Li-Bi_2WO_6, Na-Bi_2WO_6, and K-Bi_2WO_6 catalysts are $85.73°$, $67.18°$, $26.55°$, and $57.44°$ (Fig. 11), respectively. The smallest one on Na-Bi_2WO_6 evidences the full absorption toward H_2O, supporting the DFT results and suggesting the potential hydroxylation of catalytic interface. Namely, large numbers of $\bullet OH$ will be created there. Moreover, Δq is denoted as a positive value when electrons are imparted to an electron-deficient field. Hence, the higher the Δq value, the more positive charge it carries, and the easier to oxidize the toluene molecule. Exhibited as Fig. 10, the Δq values for C_7H_8, O_2, and H_2O on Na-Bi_2WO_6 are 0.46 e, 0.47 e, and 0.61 e, respectively, much higher than all the other catalysts. Overall, the optimal adsorption and activation of C_7H_8, O_2 and H_2O are rendered by Na-Bi_2WO_6, which are vital factors for achieving the deep oxidation and complete decomposition of toluene.

Given that adsorbed H_2O serve as a source of $\bullet OH$, it is indispensable to investigate the impact of relative humidity (RH) on the photocatalytic degradation of toluene under actual conditions. As Fig. 12a shows, with RH increased from 20% to 60%, the removal percentage of toluene grows from 69.8% to 80.8%, and then approaches 100% at 60% RH, as more $\bullet OH$ radicals are produced due to the increased RH. Subsequently,
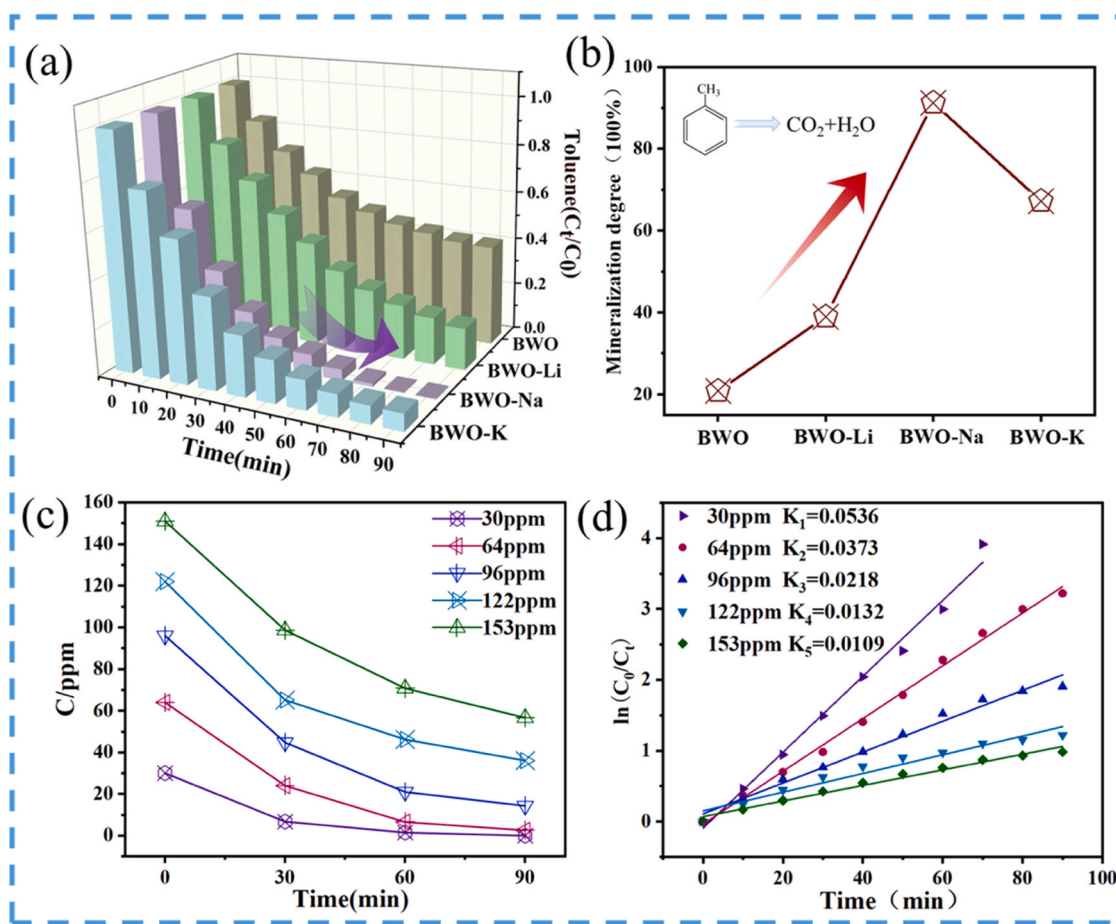
Fig. 8. (a) Residual toluene percentages over degradation time with Bi_2WO_6, $Li-Bi_2WO_6$, $Na-Bi_2WO_6$, and $K-Bi_2WO_6$ as catalysts, and (b) corresponding mineralization degree. (Initial toluene concentration:30 ppm; Illumination time:90 min.) (c) Degradation of toluene with increased initial concentration over $Na-Bi_2WO_6$, and (d) corresponding kinetic analysis.
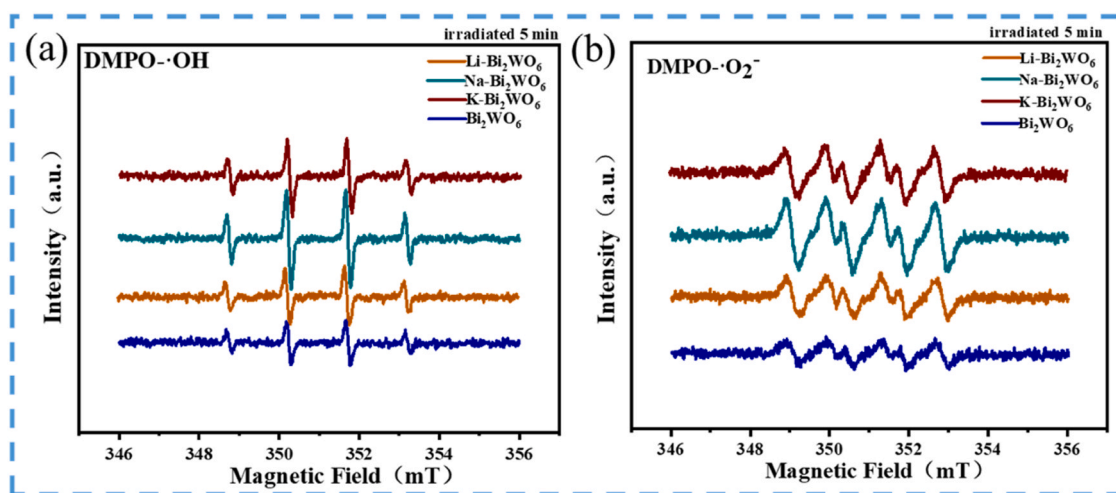

Fig. 9. DMPO spin-trapping EPR spectra of (a) •OH, and (b) •O_2^-.

a further increase in RH brings a downward trend. That's because excessive H_2O molecules compete with toluene molecules for adsorption on the porous interface of $Na-Bi_2WO_6$, restraining the absorption of toluene and thereby resulting in a dropped degradation efficiency[55].

To assess the applicability of alkalis-Bi_2WO_6, photocatalytic degradation of formaldehyde (another representative of hazardous VOCs indoors) was conducted using $Na-Bi_2WO_6$. As anticipated, 50 ppm formaldehyde can utterly be eliminated within 40 min while only about 60% removal efficiency is attained by pristine Bi_2WO_6 (Fig. 12b). Considering that toluene and formaldehyde generally coexist, the reactor was filled with 30 ppm C_7H_8, 50 ppm HCHO, and a $Na-Bi_2WO_6$ mesh (5 cm *15 cm) was placed in. Upon illumination, as shown in Fig. 12c and S12, once turned on the light, HCHO molecules decompose promptly at a rate of 0.42 ppm/min, and C_7H_8 concentration falls to 0 in
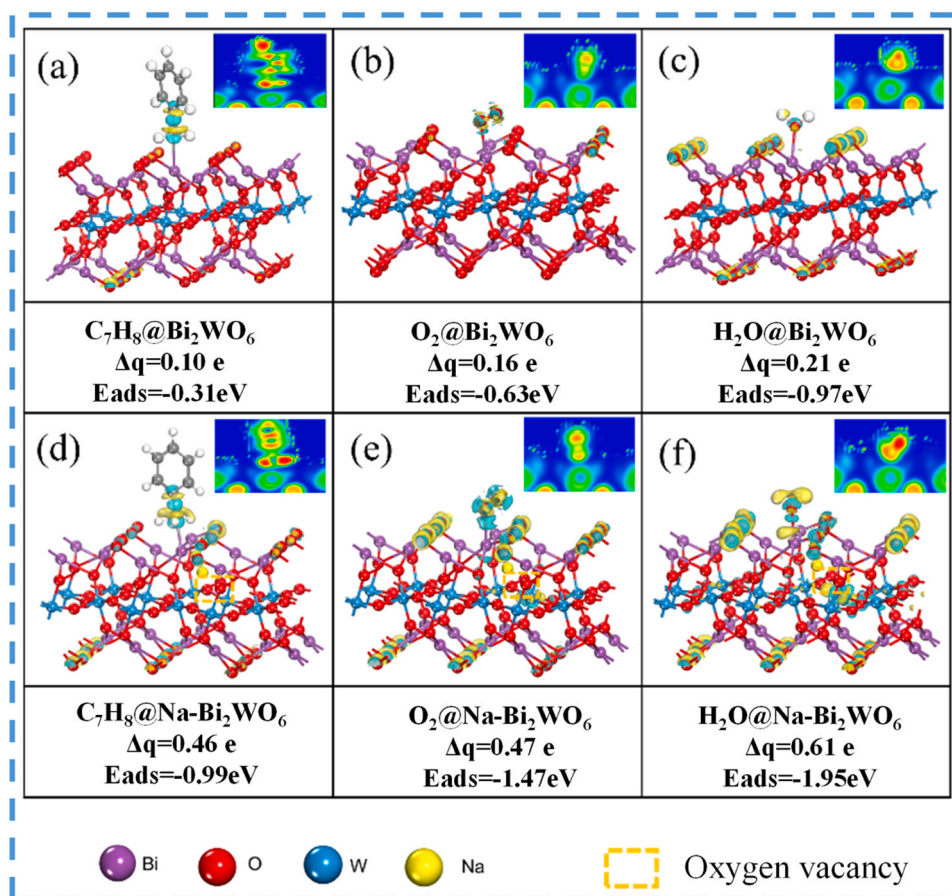
Fig. 10. Optimized C_7H_8 (toluene), O_2, and H_2O adsorption on Bi_2WO_6 (a, b, c) and Na-Bi_2WO_6(d, e, f); corresponding electron localization function diagram is in the upper right corner of each graph.
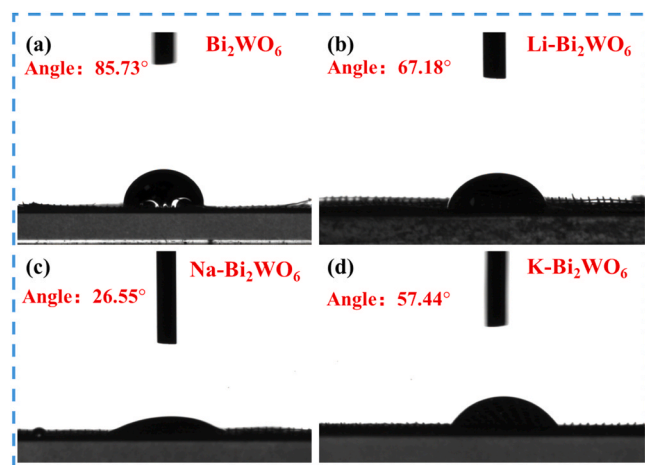
Fig. 11. Contact angle of water on (a) Bi_2WO_6, (b)Li-Bi_2WO_6, (c)Na-Bi_2WO_6, and (d) K-Bi_2WO_6.

120 min, with an associated degradation rate of 0.25 ppm/min. Fig. 12c suggests that the Na-Bi_2WO_6 mesh is high-powered and efficient in eliminating multiple indoor pollutants. Furthermore, the Na-Bi_2WO_6 mesh maintains its exceptional performance over successive runs, the efficiency in mineralize toluene just declines by 4% after 9 runs over more than 13 hours (Fig. 12d), verifying its excellent durability, which is a pivotal advance for practical application.

To verify the stability of Na-Bi_2WO_6 mesh during continuous operation, the used Na-Bi_2WO_6 after 9 repeated runs were characterized by

XRD, SEM, XPS and TEM. As shown in Fig. 13a, the crystal structure of Na-Bi_2WO_6 does not change. And its morphology maintains its original ultrathin nanosheets (Fig. 13b and c) despite the long-time reaction. Regarding the chemical state of O in Na-Bi_2WO_6, the XPS spectra in Fig. 13d depict that the O_{latt} percentage in Na-Bi_2WO_6 grows from 38.35% to 40.23% after the reaction. The same trend is observed for O_{ads} and O_{-OH} contents, with a 0.78% increase for O_{ads} and a 1.1% increase for O_{hyd}. There are slight changes, which will not affect the photocatalytic performance of Na-Bi_2WO_6. TEM images (Fig. 13e and f) also show that, the lattice spacing keeps unchanged, which is consistent with the results of XRD. Above characterization results validate the exceptional physical/chemical stability of Na-Bi_2WO_6 mesh.

Fig. S13 a-d shows the GC-MS spectra associating with the intermediates produced during degradation in the presence of Na-Bi_2WO_6. Identified intermediates include Benzyl alcohol, benzaldehyde, benzoic acid, p-hydroxybenzoic acid, 2,4-dihydroxybenzoic acid, and 5-hydroxy-2-(hydroxymethyl) pentanoic acid. Based on this analysis, the degradation path is proposed according to the generation sequence of the intermediates (Fig. S13e).

Being adsorbed on the porous Na-Bi_2WO_6, the activated toluene molecules are subjected to the surrounding •OH and •O_2^-. Then •OH initiates the degradation of toluene[36]. As shown, the methyl carbon on toluene is attacked by •OH to form benzyl alcohol, which is oxidized to benzaldehyde by •O_2^-, and then oxidized to benzoic acid. On account of the electron-donating capacity of -COOH and the steric hindrance, the para position of benzoic acid is most susceptible to •OH attack, producing para-hydroxybenzoic acid. Then -OH is grafted on the ortho-position of benzoic acid, generating 2,4-dihydroxybenzoic acid due to the substitute rule on benzene ring. In 2, 4-dihydroxybenzoic acid, both -COOH and -OH donate electrons to the benzene ring and
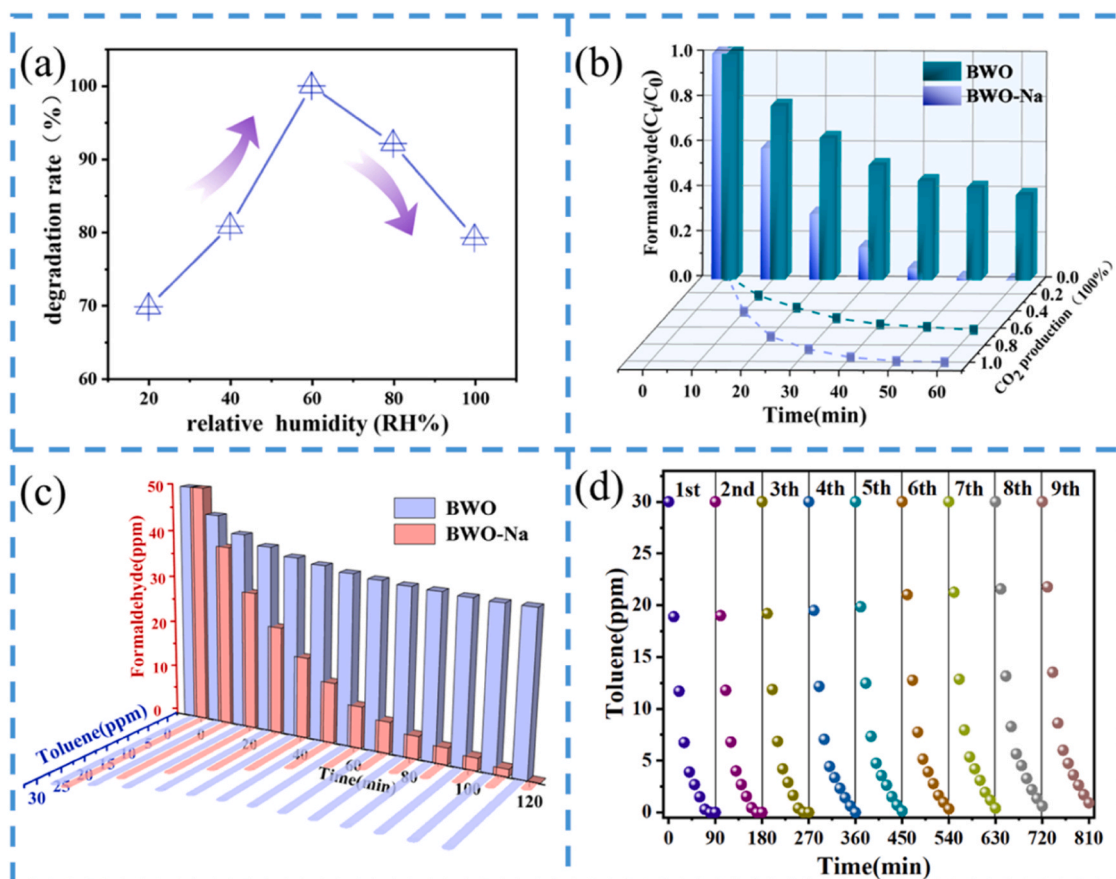
Fig. 12. (a) Degradation of toluene under different relative humidity, (b) elimination of formaldehyde on Bi_2WO_6 and $Na-Bi_2WO_6$, (c) degradation of coexistent toluene and formaldehyde, (d) 9 runs of toluene degradation performed on $Na-Bi_2WO_6$.

thicken the electron density along carbon skeleton, which makes the benzene ring ready to accept the attack from $\bullet O_2^-$ and $\bullet OH$. Consequently, the benzene ring is cleaved, producing 5-hydroxy-2-(hydroxymethyl) pentanoic acid, which is ultimately converted into CO_2 and H_2O.

As there are abundant ROS on $Na-Bi_2WO_6$ mesh, its effectiveness in the photocatalytic disinfection of bacteria was assessed. To specifically highlight the antimicrobial properties of $Na-Bi_2WO_6$, the catalyst powders were scraped off from the W skeleton and collected for testing, corresponding details of the antimicrobial test are given in Experimental section. The blank group and the control group were set up to exclude the influence of light and the catalyst in the absence of light irradiation. As shown in Fig. 14a and b, the controlled groups with and without catalysts display that no deactivation of both *E. coli* and *S. aureus* is observed, indicating that the non-toxic nature of $Na-Bi_2WO_6$ towards these bacteria. In the control groups, the colonies do not decrease under light irradiation, proving that light alone can't kill bacteria. However, once turn on the lights and mix the $Na-Bi_2WO_6$ powders in culture medium, a large number of bacterial colonies are deactivated, illustrating that the excited $Na-Bi_2WO_6$ has an impressive antibacterial effect on gram-negative bacteria (*E. coli*) and gram-positive bacteria (*S. aureus*). The antibacterial experiment of $Na-Bi_2WO_6$ photocatalyst was carried out again, and the inactivation efficiency was calculated by referring the methods reported in related pioneering studies[57,58]. The inactivation efficiency of $Na-Bi_2WO_6$ on *E. coli* and *S. aureus* is 67.6% and 93.2%, respectively. It is proved that $Na-Bi_2WO_6$ photocatalyst can effectively kill bacteria. Above findings underscore that the $Na-Bi_2WO_6$ mesh is auspicious in improving indoor air quality by eliminating harmful bacteria.

3.5. Designing a portable air purifier with $Na-Bi_2WO_6$ mesh

As quality of life improves, people are increasingly focused on physical health, particularly the requirements for high air quality. For office workers, especially those who spend prolonged time at their computer desks, a portable air purifier that can supply fresh and safe air on demand is likely to be well-received. To address this need, a cup-shaped portable photocatalyst air purifier was designed and assembled. Standing at 120 mm in height and 80 mm in diameter, this device is suitable for office desktop within a 2 m^3 range, a conventional space for a carrel. All the necessary supports were 3D printed using rigid resin as precursors.

As shown in Fig. 15a and b, the purifier comprises three parts. The top section features a fan and four lithium batteries. The fan functions to draw in air to ensure the air circulation within the purifier, and the lithium batteries provide a 3-hour operating capacity. The middle part houses the photocatalyst unit, which includes photocatalyst-holding platform, an LED light strip (Length: 37.5 cm; Light density: 20 W/m^2) and $Na-Bi_2WO_6/W$ mesh. The bottom section is equipped with a HEPA filter to screen off particles. Due to the lacking of a large test box, air purification tests were conducted in a sealed 120 dm^3 box to verify the practicality of the portable air purifier (Fig. S14). Detailed test procedures are outlined in the SI file. The designed portable air purifier can degrade 2 ppm (2.68 mg/m^3) formaldehyde and 1 ppm (4.11 mg/m^3) toluene by over 98% within 60 minutes (Fig. 15c). The final pollutant concentrations are lower than the national standard limits of 0.2 mg/m^3 for toluene and 0.08 mg/m^3 for formaldehyde, respectively[59]. In terms of disinfection efficacy (Fig. 15d), the OD600 absorbance decreases from 1.91 to 0.76, indicating a significant reduction in bacterial presence in the enclosed space after 1 hour of purification. The
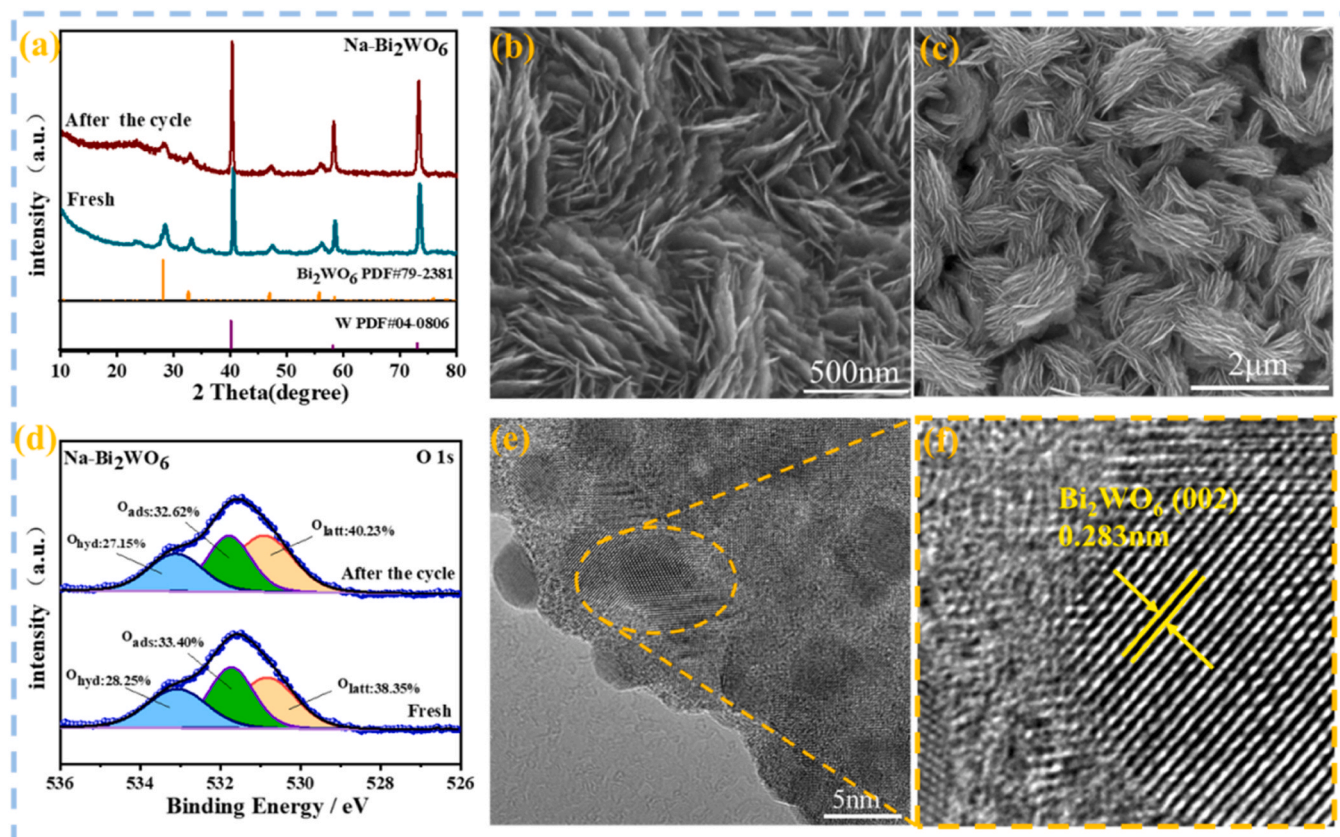
Fig. 13. (a) XRD patterns of fresh Na-Bi$_2$WO$_6$ and used Na-Bi$_2$WO$_6$ after the repeated runs; (b, c) corresponding SEM images; (d) High-resolution XPS spectra; (e, f) HRTEM images of used Na-Bi$_2$WO$_6$.
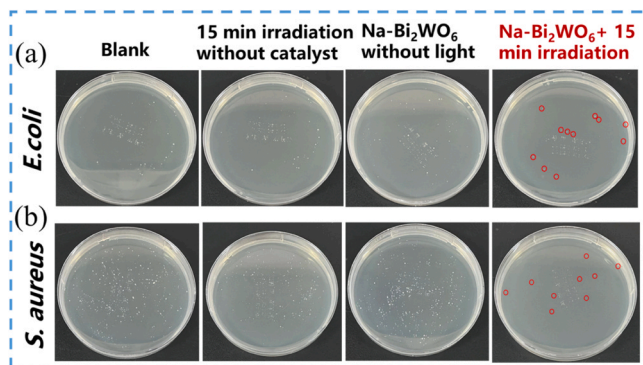

Fig. 14. Photocatalytic disinfection of bacteria: (a) *E. coli* and (b) *S. aureus* under visible light irradiation. Experimental conditions: powdery photocatalyst: 10 mg, initial bacterial volume: 50 μL, light intensity: 138 mW/cm^2.

Na-Bi$_2$WO$_6$ mesh demonstrates an antibacterial rate of approximately 60.2%, highlighting the air purifier has a good disinfection capability. Fig. 15e depicts a scheme illustrating the crystal splitting of Bi$_2$WO$_6$ nanoflakes, and the capacity of transforming toluene in H$_2$O and CO$_2$, killing bacteria as well. Fig. 15f shows that the portable air purifier can be used in daily life as the simulated real-world application scenario depicts.

4. Conclusions

Na$^+$ enabling ultra-laminar splitting of Bi$_2$WO$_6$ and the final photocatalytic activity were revealed for the first time. A common Bi$_2$WO$_6$ nanoflake can further split in multiple ultrathin layers due to the intercalation effect from Na$^+$. Comparative studies on the function of Li$^+$ and K$^+$ indicate that Na$^+$ renders the best construction and photocatalytic performance of Bi$_2$WO$_6$. The resultant Na-Bi$_2$WO$_6$ nanoflakes, enriched with oxygen vacancy, grow in-situ on a W mesh, which is an ideal self-supporting photocatalyst for eliminating VOCs and indoor bacteria. Research findings and computational calculation validate that the plentiful oxygen vacancies serve as electron-trap centers for rendering the strengthened adsorption and activation of toluene, H$_2$O, and O$_2$. Fueled by visible lights, abundant •OH and •O$_2^-$ are created, empowering the Na-Bi$_2$WO$_6$ efficient in mineralizing toluene in CO$_2$ and H$_2$O without producing any toxic intermediates, which also demonstrate exceptional efficacy in degrading formaldehyde and disinfecting the environment.

On the strength of the highly photocatalytic activity, exceptional durability, and structural robustness, the Na-Bi$_2$WO$_6$ mesh emerges as a promising candidate for improving air quality, which structural integrity can streamline the manufacturing process and shorten the distance between academic research and practical application.

CRediT authorship contribution statement

Shenglian Luo: Resources. **Jianping Zou:** Resources, Conceptualization. **Weili Dai:** Project administration. **Qi Wang:** Investigation. **Ziyi Wu:** Investigation. **Lixia Yang:** Writing – review & editing, Supervision. **Mingxia Lu:** Writing – original draft, Methodology, Investigation. **Renjie Song:** Methodology. **Shuqu Zhang:** Methodology. **Jiajian Xu:** Investigation. **Menglei Wang:** Conceptualization.

Declaration of Competing Interest

We declare that we have no known competing financial interests or personal relationships that could have appeared to influence the work
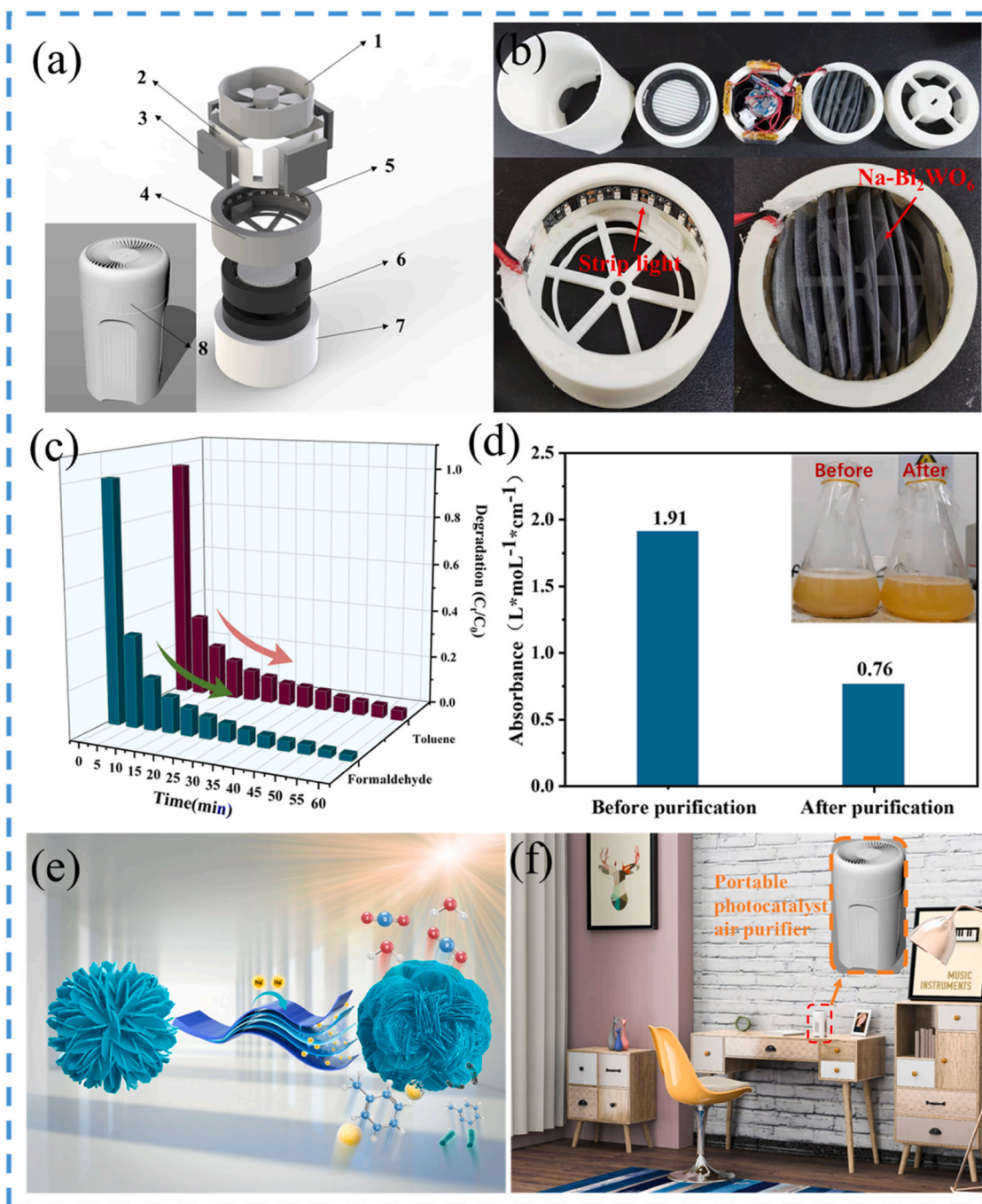
Fig. 15. (a) Structural diagram of a portable air purifier (1-fan, 2-battery and fan bearing structure, 3-lithium battery, 4-photocatalyst carrier platform, 5-strip light, 6-HEPA, 7-base , 8-Designed purifier housing). (b) 3D printed portable air purifier. (c) Test results of a 3D printed air purifier on formaldehyde and toluene in a simulation box. (d) Disinfection effect of 3D printed air purifier working in a simulation box. (e) Mechanism diagram of Na-Bi$_2$WO$_6$ catalyst for toluene degradation and disinfection. (f) virtual usage scenarios of our portable air purifier.

reported in this manuscript (Title: An all-in-one self-supporting Na-Bi$_2$WO$_6$ photocatalyst for portable air purifier: Laminar splitting boosts high efficacy in mineralizing toluene and disinfection.)

Data Availability

Data will be made available on request.

Acknowledgments

Appendix A. Supporting information

Supplementary data associated with this article can be found in the online version at doi:10.1016/j.apcatb.2024.124134.

References

[1] W.B. Li, J.X. Wang, H. Gong, Catalytic combustion of VOCs on non-noble metal catalysts, Catal. Today 148 (2009) 81–87, https://doi.org/10.1016/j. cattod.2009.03.007.

[2] X. Qiao, M. Sun, Y. Wang, D. Zhang, R. Zhang, B. Zhao, J. Zhang, Strong relations of peroxyacetyl nitrate (PAN) formation to alkene and nitrous acid during various episodes, Environ. Pollut. 326 (2023) 121465, https://doi.org/10.1016/j. envpol.2023.121465.

[3] R. Chen, J. Li, H. Wang, P. Chen, Xa Dong, Y. Sun, Y. Zhou, F. Dong, Photocatalytic reaction mechanisms at a gas–solid interface for typical air pollutant decomposition, J. Mater. Chem. A 9 (2021) 20184–20210, https://doi.org/ 10.1039/d1ta03705f.

[4] Z. Zhao, S. Ma, B. Gao, F. Bi, R. Qiao, Y. Yang, M. Wu, X. Zhang, A systematic review of intermediates and their characterization methods in VOCs degradation by different catalytic technologies, Sep. Purif. Technol. 314 (2023) 123510, https://doi.org/10.1016/j.seppur.2023.123510.

[5] S. Weon, J. Kim, W. Choi, Dual-components modified TiO₂ with Pt and fluoride as deactivation-resistant photocatalyst for the degradation of volatile organic compound, Appl. Catal. B 220 (2018) 1–8, https://doi.org/10.1016/j. apcatb.2017.08.036.

[6] S.M.T. Salthammer, Formaldehyde in the Indoor Environment, Chem. Rev. 110 (2010) 2536–2572, https://doi.org/10.1021/cr800399g.

[7] A.B.N.C.H.J. Malmiri, Volatile Organic Compounds Removal Methods: A Review, Am. J. Biochem Biotechnol. 8 (4) (2012) 220–229, https://doi.org/10.3844/ ajbbsp.2012.220.229.

[8] J. Tian, Y. Sang, G. Yu, H. Jiang, X. Mu, H. Liu, A. Bi2WO6, -based hybrid photocatalyst with broad spectrum photocatalytic properties under UV, visible, and near-infrared irradiation, Adv. Mater. 25 (2013) 5075–5080, https://doi.org/ 10.1002/adma.201302014.

[9] J. Jia, F. Qin, J. Guo, Z. Liu, Q. Zhao, W. Guan, FeOOH coupled Bi2WO6 for efficient photocatalysis-Fenton synergistic degradation of organic pollutants, Mater. Lett. 336 (2023) 133862, https://doi.org/10.1016/j.matlet.2023.133862.

[10] J. Dong, J. Hu, A. Liu, J. He, Q. Huang, Y. Zeng, W. Gao, Z. Yang, Y. Zhang, Y. Zhou, Z. Zou, Simple fabrication of Z-scheme MgIn₂S₄/Bi₂WO₆ hierarchical heterostructures for enhancing photocatalytic reduction of Cr(VI), Catal. Sci. Technol. 11 (2021) 6271–6280, https://doi.org/10.1039/d1cy01178b.

[11] M. Ahmadi, S.M. Alavi, A. Larimi, UV–vis light responsive Bi₂WO₆ nanosheet/TiO₂ nanobelt heterojunction photocatalyst for CO₂ reduction, Catal. Commun. 179 (2023) 106681, https://doi.org/10.1016/j.catcom.2023.106681.

[12] Y.Q. Wang, S. Jiang, F. Liu, C.C. Zhao, D.F. Zhao, X.F. Li, Study on preparation and toluene removal of BiOI/Bi₂WO₆/ACF photocatalyst, Appl. Surf. Sci. 488 (2019) 161–169, https://doi.org/10.1016/j.apsusc.2019.05.228.

[13] J. Yang, L. Yang, M. Fang, L. Li, F. Fu, H. Xu, M.G. Li, X.M. Fan, A compact Z-scheme heterojunction of BiOCl/Bi₂WO₆ for efficiently photocatalytic degradation of gaseous toluene, J. Colloid Interface Sci. 631 (2023) 44–54, https://doi.org/ 10.1016/j.jcis.2022.11.023.

[14] J. Yang, L. Li, F. Fu, H. Xu, K. Da, S.B. Cao, W.T. Chen, L. Yang, X.M. Fan, Construction of Z-scheme Ag/AgCl/Bi₂WO₆ photocatalysts with enhanced visible-light photocatalytic performance for gaseous toluene degradation, Appl. Surf. Sci. 610 (2023) 155598, https://doi.org/10.1016/j.apsusc.2022.155598.

[15] Y. Jia, X. Zhang, R.Y. Wang, J. Yuan, R.Z. Zheng, J.Q. Zhang, F.P. Qian, Y.F. Chen, M. Zhang, L.A. Guo, Energy band engineering of WO₃/Bi₂WO₆ direct Z-scheme for enhanced photocatalytic toluene degradation, Appl. Surf. Sci. 618 (2023) 156636, https://doi.org/10.1016/j.apsusc.2023.156636.

[16] M.L. Wang, H. Xiao, Y.X. Ru, L.X. Yang, W. Liu, T.Z. Ma, L.M. Yang, S.Q. Zhang, W. L. Dai, In₂S₃ nanoflakes grounded in Bi₂WO₆ nanoplates: A novel hierarchical heterojunction catalyst anchored on W mesh for efficient elimination of toluene, Environ. Res. Lett. 212 (2022) 113148, https://doi.org/10.1016/j. envres.2022.113148.

[17] S. Luo, J. Ke, M.Q. Yuan, Q. Zhang, P. Xie, L.D. Deng, S.B. Wang, CuInS₂ quantum dots embedded in Bi₂WO₆ nanoflowers for enhanced visible light photocatalytic removal of contaminants, Appl. Catal. B 221 (2018) 215–222, https://doi.org/ 10.1016/j.apcatb.2017.09.028.

[18] X. Yang, Y. Ma, Y. Liu, K. Wang, Y. Wang, M. Liu, X. Qiu, W. Li, J. Li, Defect-Induced Ce-Doped Bi₂WO₆ for Efficient Electrocatalytic N₂ Reduction, ACS Appl. Mater. Interfaces 13 (2021) 19864–19872, https://doi.org/10.1021/ acsami.0c22623.

[19] X. Li, W. Li, S. Gu, X. Liu, H. Li, C. Ren, X. Ma, H. Zhou, Efficient ytterbium-doped Bi₂WO₆ photocatalysts: Synthesis, the formation of oxygen vacancies and boosted superoxide yield for enhanced visible-light photocatalytic activity, J. Alloy. Compd. 851 (2021) 156935, https://doi.org/10.1016/j.jallcom.2020.156935.

[20] V. Koteski, J. Belošević-Čavor, V. Ivanovski, A. Umićević, D. Toprek, Abinitio calculations of the optical and electronic properties of Bi₂WO₆ doped with Mo, Cr, Fe, and Zn on the W–lattice site, Appl. Surf. Sci. 515 (2020) 146036, https://doi. org/10.1016/j.apsusc.2020.146036.

[21] V. Maddineni, F.M. Ali, H. Ibrahim, Efficient photocatalytic removal of N-nitrosamines from amine washing wastewater using bismuth tungstate, Can. J. Chem. Eng. (2023), https://doi.org/10.1002/cjce.24900.

[22] L. Liu, J. Liu, K. Sun, J. Wan, F. Fu, J. Fan, Novel phosphorus-doped Bi₂WO₆ monolayer with oxygen vacancies for superior photocatalytic water detoxication and nitrogen fixation performance, Chem. Eng. J. 411 (2021) 128629, https://doi. org/10.1016/j.cej.2021.128629.

[23] J. Zhang, P. Deng, M. Deng, H. Shen, Z. Feng, H. Li, Hybrid Density Functional Theory Study of Native Defects and Nonmetal (C, N, S, and P) Doping in a Bi₂WO₆

[24] H. Yu, C. Chu, X. An, Enhanced visible-light-driven photocatalytic activity of F doped reduced graphene oxide - Bi₂WO₆ photocatalyst, Appl. Organomet. Chem. 33 (2019) e4682, https://doi.org/10.1002/aoc.4682.

[25] A. Waehayee, C. Duangkamol, M. Chotsawat, T. Lerdwiriyanupap, T. Pewklang, H. Nakajima, T. Butburee, A. Kamkaew, S. Suthirakun, T. Siritanon, Controlling the Photocatalytic Activity and Benzylamine Photooxidation Selectivity of Bi₂WO₆ via Ion Substitution: Effects of Electronegativity, Inorg. Chem. 62 (2023) 3506–3517, https://doi.org/10.1021/acs.inorgchem.2c03860.

[26] A. Kumar, S. Kashyap, M. Sharma, V. Krishnan, Tuning the surface and optical properties of graphitic carbon nitride by incorporation of alkali metals (Na, K, Cs and Rb): Effect on photocatalytic removal of organic pollutants, Chemosphere 287 (2022) 131988, https://doi.org/10.1016/j.chemosphere.2021.131988.

[27] Y. Zhou, Y. Zhang, M. Lin, J. Long, Z. Zhang, H. Lin, J.C. Wu, X. Wang, Monolayered Bi₂WO₆ nanosheets mimicking heterojunction interface with open surfaces for photocatalysis, Nat. Commun. 6 (2015) 8340, https://doi.org/ 10.1038/ncomms9340.

[28] C.C.Y. Zheng, Y. Zhan, X. Lin, Q. Zheng, K. Wei, J. Zhu, Y. Zhu, Luminescence and Photocatalytic Activity of ZnO Nanocrystals: Correlation between Structure and Property, Inorg. Chem. 46 (2006) 6675–6682, https://doi.org/10.1021/ ic062394m.

[29] C-N.L.T.-J. Kuo, C.-L. Kuo, M.H. Huang, Growth of Ultralong ZnO Nanowires on Silicon Substrates by Vapor Transport and Their Use as Recyclable Photocatalysts, Chem. Mater. 19 (2007) 5143–5147, https://doi.org/10.1021/cm071568a.

[30] B. Han, Y.C. Zou, Z. Zhang, X.M. Yang, X.B. Shi, H. Meng, H. Wang, K. Xu, Y. H. Deng, M. Gu, Probing the Na metal solid electrolyte interphase via cryo-transmission electron microscopy, Nat. Commun. 12 (2021) 3066, https://doi.org/ 10.1038/s41467-021-23368-6.

[31] P. Zhang, T. Wang, X. Chang, J. Gong, Effective Charge Carrier Utilization in Photocatalytic Conversions, Acc. Chem. Res. 49 (2016) 911–921, https://doi.org/ 10.1021/acs.accounts.6b00036.

[32] Y. Cui, T. Wang, J. Liu, L. Hu, Q. Nie, Z. Tan, H. Yu, Enhanced solar photocatalytic degradation of nitric oxide using graphene quantum dots/bismuth tungstate composite catalysts, Chem. Eng. J. 420 (2021) 129595, https://doi.org/10.1016/j. cej.2021.129595.

[33] Z. Kang, E. Lin, N. Qin, J. Wu, D. Bao, Bismuth Vacancy-Mediated Quantum Dot Precipitation to Trigger Efficient Piezocatalytic Activity of Bi₂WO₆ Nanosheets, ACS Appl. Mater. Interfaces 14 (2022) 11375–11387, https://doi.org/10.1021/ acsami.1c23282.

[34] H.W. Huang, K. Liu, K. Chen, Y.L. Zhang, Y.H. Zhang, S.C. Wang, Ce and F Comodification on the Crystal Structure and Enhanced Photocatalytic Activity of Bi₂WO₆ Photocatalyst under Visible Light Irradiation, J. Phys. Chem. C 118 (2014) 14379–14387, https://doi.org/10.1021/jp503025b.

[35] Y.-Y. Guo, W.-B. Zhang, Y.-N. Yang, C. Wang, The photocatalytic efficiency enhancement of Bi₄O₅Br₂ by Li-intercalation for NO removal, J. Phys. Chem. Solids 159 (2021) 110256, https://doi.org/10.1016/j.jpcs.2021.110256.

[36] L. Yang, J. Guo, J. Zhang, S. Zhang, W. Dai, X. Xiao, X. Luo, S. Luo, Utter degradation of toluene with inhibiting the generation of benzene by self-supporting Bi₂MoO₆ nanoflakes featuring OV-enriched interface, Chem. Eng. J. 427 (2022) 131550, https://doi.org/10.1016/j.cej.2021.131550.

[37] T. Wang, C. Feng, J. Liu, D. Wang, H. Hu, J. Hu, Z. Chen, G. Xue, Bi₂WO₆ hollow microspheres with high specific surface area and oxygen vacancies for efficient photocatalysis N₂ fixation, Chem. Eng. J. 414 (2021) 128827, https://doi.org/ 10.1016/j.cej.2021.128827.

[38] H. Zhang, J. Li, L. Luo, J. Zhao, J. He, X. Zhao, H. Liu, Y. Qin, F. Wang, J. Song, Hierarchically porous MXene decorated carbon coated LiFePO₄ as cathode material for high-performance lithium-ion batteries, J. Alloy. Compd. 876 (2021) 160210, https://doi.org/10.1016/j.jallcom.2021.160210.

[39] W. Kong, Z. Xing, B. Fang, Y. Cui, Z. Li, W. Zhou, Plasmon Ag/Na-doped defective graphite carbon nitride/NiFe layered double hydroxides Z-scheme heterojunctions toward optimized photothermal-photocatalytic-Fenton performance, Appl. Catal. B 304 (2022) 120969, https://doi.org/10.1016/j.apcatb.2021.120969.

[40] R. Li, L. Liu, B. Ming, Y. Ji, R. Wang, Oxygen vacancy effect on photoluminescence of KNb₃O₈ nanosheets, Appl. Surf. Sci. 439 (2018) 983–990, https://doi.org/ 10.1016/j.apsusc.2017.12.218.

[41] Y. Zhou, Z. Tian, Z. Zhao, Q. Liu, J. Kou, X. Chen, J. Gao, S. Yan, Z. Zou, High-yield synthesis of ultrathin and uniform Bi₂WO₆ square nanoplates benefitting from photocatalytic reduction of CO₂ into renewable hydrocarbon fuel under visible light, ACS Appl. Mater. Interfaces 3 (2011) 3594–3601, https://doi.org/10.1021/ am2008147.

[42] T. Lu, Y. Gao, Y. Yang, H. Ming, Z. Huang, G. Liu, D. Zheng, J. Zhang, Y. Hou, Efficient degradation of tetracycline hydrochloride by photocatalytic ozonation over Bi₂WO₆, Chemosphere 283 (2021) 131256, https://doi.org/10.1016/j. chemosphere.2021.131256.

[43] Z. Sun, Y. Jiang, W. Wang, R. Zhong, Y. Pu, Q. Chen, B. Nan, J. He, L. Huang, Visible-light-stimulated Alkalis-triggered Platinum Cocatalyst with Electron Deficient Interface for Hydrogen Evolution, ChemCatChem 12 (2020) 2189–2193, https://doi.org/10.1002/cctc.201902370.

[44] H.S. Shim, J.W. Kim, Y.E. Sung, W.B. Kim, Electrochromic properties of tungsten oxide nanowires fabricated by electrospinning method, Sol. Energy Mater. Sol. Cells 93 (2009) 2062–2068, https://doi.org/10.1016/j.solmat.2009.02.008.

[45] J.Y. Zheng, G. Song, J.S. Hong, T.K. Van, A.U. Pawar, D.Y. Kim, C.W. Kim, Z. Haider, Y.S. Kang, Facile Fabrication of WO₃ Nanoplates Thin Films with Dominant Crystal Facet of (002) for Water Splitting, Cryst. Growth Des. 14 (2014) 6057–6066, https://doi.org/10.1021/cg5012154.

Photocatalyst, Acs Omega 5 (2020) 29081–29091, https://doi.org/10.1021/ acsomega.0c03685.

[46] W. Liu, M. Shi, Y. Li, Z. Wu, L. Yang, S. Zhang, X. Xiao, C. Liu, W. Dai, C. Chen, X. Tu, J. Zou, X. Luo, Congregated-electrons-strengthened anchoring and mineralization of gaseous formaldehyde on a novel self-supporting $Cu_{2-x}Se/Cu_2O$ heterojunction photocatalyst under visible lights: A viable mesh for designing air purifier, Appl. Catal. B 312 (2022) 121427, https://doi.org/10.1016/j.apcatb.2022.121427.

[47] N. Tian, C. Hu, J. Wang, Y. Zhang, T. Ma, H. Huang, Layered bismuth-based photocatalysts, Coord. Chem. Rev. 463 (2022) 214515, https://doi.org/10.1016/j.ccr.2022.214515.

[48] J.J. Li, M. Zhang, B. Weng, X. Chen, J. Chen, H.P. Jia, Oxygen vacancies mediated charge separation and collection in Pt/WO_3 nanosheets for enhanced photocatalytic performance, Appl. Surf. Sci. 507 (2020) 145133, https://doi.org/10.1016/j.apsusc.2019.145133.

[49] Y.Y. Qin, H. Li, J. Lu, Y.C. Ding, C.C. Ma, X.L. Liu, M.J. Meng, Y.S. Yan, Fabrication of Bi_2WO_6/In_2O_3 photocatalysts with efficient photocatalytic performance for the degradation of organic pollutants: Insight into the role of oxygen vacancy and heterojunction, Adv. Powder Technol. 31 (2020) 2890–2900, https://doi.org/10.1016/j.apt.2020.05.014.

[50] X.Y. Jin, S.Y. Lei, J.F. Chen, J.B. Zhong, S.L. Zhang, X.Q. Tang, Bi^0 and oxygen vacancies co-induced enhanced visible-light photocatalytic detoxication of three typical contaminants over Bi_2WO_6 treated by $NaBH_4$ solution, Surf. Interfaces 28 (2022) 101648, https://doi.org/10.1016/j.surfin.2021.101648.

[51] P. Li, H. Tang, T. Li, X. Li, X. Shao, T. Pavelka, L. Huang, H. Gong, Measuring the Minority-Carrier Diffusion Length of n-Type $In_{0.53}Ga_{0.47}As$ Epilayers Using Surface Photovoltage, J. Electron. Mater. 46 (2017) 2061–2066, https://doi.org/10.1007/s11664-016-5124-y.

[52] W.L. Dai, M.L. Zou, C. Zhao, J. Zhang, L. Wang, X.S. Wang, L.X. Yang, L. Zhou, J.P. Zou, X.B. Luo, S.L. Luo, G.H. Jing, Monoatomic oxygen fueled by oxygen vacancies governs the photothermocatalytic deep oxidation of toluene on Na-doped Co_3O_4, Appl. Catal. B-Environ. 317 (2022), https://doi.org/10.1016/j.apcatb.2022.121769.

[53] Z. Xie, Y. Xu, D. Li, S. Meng, M. Chen, D. Jiang, Covalently Bonded Bi_2O_3 Nanosheet/Bi_2WO_6 Network Heterostructures for Efficient Photocatalytic CO_2 Reduction, ACS Appl. Energy Mater. 3 (2020) 12194–12203, https://doi.org/10.1021/acsaem.0c02252.

[54] X. Cao, A. Huang, C. Liang, H.C. Chen, T. Han, R. Lin, Q. Peng, Z. Zhuang, R. Shen, H.M. Chen, Y. Yu, C. Chen, Y. Li, Engineering Lattice Disorder on a Photocatalyst: Photochromic BiOBr Nanosheets Enhance Activation of Aromatic C-H Bonds via Water Oxidation, J. Am. Chem. Soc. 144 (2022) 3386–3397, https://doi.org/10.1021/jacs.1c10112.

[55] L. Yang, J. Guo, T. Yang, C. Guo, S. Zhang, S. Luo, W. Dai, B. Li, X. Luo, Y. Li, Self-assembly Cu_2O nanowire arrays on Cu mesh: A solid-state, highly-efficient, and stable photocatalyst for toluene degradation under sunlight, J. Hazard. Mater. 402 (2021) 123741, https://doi.org/10.1016/j.jhazmat.2020.123741.

[56] Y.S.L. Luo, High efficient photocatalytic degradation of p-nitrophenol on a unique Cu_2O/TiO_2 p-n heterojunction network catalyst, Environ. Sci. Technol. 44 (2010) 7641–7646, https://doi.org/10.1021/es101711k.

[57] L.H. Peng, H.Y. Wang, G.Y. Li, W.P. Zhang, Z.S. Liang, T.C. An, Photocatalytic inactivation of airborne bacteria onto g-C_3N_4/TiO_2/Ni-polydopamine/Ni bifunctional coupling filter with non-size dependent capture effect, Appl. Catal. B 329 (2023) 122580, https://doi.org/10.1016/j.apcatb.2023.122580.

[58] H.Y. Wang, L.H. Peng, G.Y. Li, W.P. Zhang, Z.S. Liang, H.J. Zhao, T.C. An, Photocatalytic ozonation inactivation of bioaerosols by NiFeOOH nanosheets in situ grown on nickel foam, Appl. Catal. B 324 (2023) 122273, https://doi.org/10.1016/j.apcatb.2022.122273.

[59] Y. Lu, A Novel Indoor Air Quality Standards and Design Methods in Environmental Assessment, J. Phys. Conf. Ser. 1549 (2020) 022083, https://doi.org/10.1088/1742-6596/1549/2/022083.